

# Combiner and HyperCombiner Networks: Rules to Combine Multimodality MR Images for Prostate Cancer Localisation

Wen Yan<sup>a,b,c,\*</sup>, Bernard Chiu<sup>a</sup>, Ziyi Shen<sup>b,c</sup>, Qianye Yang<sup>b,c</sup>, Tom Syer<sup>d</sup>, Zhe Min<sup>b,c</sup>, Shonit Punwani<sup>d</sup>, Mark Emberton<sup>d</sup>, David Atkinson<sup>e</sup>, Dean C. Barratt<sup>b,c</sup>, Yipeng Hu<sup>b,c</sup>

<sup>a</sup>Department of Electrical Engineering, City University of Hong Kong, 83 Tat Chee Avenue, Hong Kong, China

<sup>b</sup>Department of Medical Physics & Biomedical Engineering, University College London, Gower St, London WC1E 6BT, London, U.K.

<sup>c</sup>Wellcome/EPSCRC Centre for Interventional and Surgical Sciences, University College London, Gower St, London WC1E 6BT, London, U.K.

<sup>d</sup>Centre for Medical Imaging, Division of Medicine, University College London, Foley Street W1W 7TS, London, U.K.

<sup>e</sup>Division of Surgery & Interventional Science, University College London, Gower St, London WC1E 6BT, London, U.K.

---

## Abstract

One of the distinct characteristics in radiologists' reading of multiparametric prostate MR scans, using reporting systems such as PI-RADS v2.1, is to score individual types of MR modalities, T2-weighted, diffusion-weighted, and dynamic contrast-enhanced, and then combine these image-modality-specific scores using standardised decision rules to predict the likelihood of clinically significant cancer. This work aims to demonstrate that it is feasible for low-dimensional parametric models to model such decision rules in the proposed Combiner networks, without compromising the accuracy of predicting radiologic labels: First, it is shown that either a linear mixture model or a nonlinear stacking model is sufficient to model PI-RADS decision rules for localising prostate cancer. Second, parameters of these (generalised) linear models are proposed as hyperparameters, to weigh multiple networks that independently repre-

---

\*Corresponding author: Tel.: +852-53416639

Email addresses: wenyang6-c@my.cityu.edu.hk (Wen Yan), bcychiu@cityu.edu.hk (Bernard Chiu), ziyi-shen@ucl.ac.uk (Ziyi Shen), qianye.yang.19@ucl.ac.uk (Qianye Yang), t.syer@ucl.ac.uk (Tom Syer), z.min@ucl.ac.uk (Zhe Min), s.punwani@ucl.ac.uk (Shonit Punwani), m.emberton@ucl.ac.uk (Mark Emberton), d.atkinson@ucl.ac.uk (David Atkinson), d.barratt@ucl.ac.uk (Dean C. Barratt), yipeng.hu@ucl.ac.uk (Yipeng Hu)

sent individual image modalities in the Combiner network training, as opposed to end-to-end modality ensemble. A HyperCombiner network is developed to train a single image segmentation network that can be conditioned on these hyperparameters during inference, for much improved efficiency. Experimental results based on data from 850 patients, for the application of automating radiologist labelling multi-parametric MR, compare the proposed combiner networks with other commonly-adopted end-to-end networks. Using the added advantages of obtaining and interpreting the modality combining rules, in terms of the linear weights or odds-ratios on individual image modalities, three clinical applications are presented for prostate cancer segmentation, including modality availability assessment, importance quantification and rule discovery.

*Keywords:*

Decision rule modelling, prostate cancer localisation, combiner networks, multiparametric MRI

---

## **1. Introduction**

The use of Multi-parametric magnetic resonance (mpMR) images comprised of T2-weighted (T2W), diffusion-weighted imaging (DWI) including its high b-value weighting ( $DWI_{hb}$ ) and apparent diffusion coefficient (ADC) maps, together with dynamic contrast-enhanced (DCE) modalities, is recommended by multiple national guidelines for the initial investigation of patients with suspected prostate cancer (Turkbey et al., 2011; Haider et al., 2007) and reducing unnecessary invasive biopsy and treatment of prostate cancer (Ahmed et al., 2017). Recommended scoring systems for lesion localisation on mpMR images include the Prostate Imaging Reporting Data System (PI-RADS) and Likert scale. PI-RADS guidance (v1) (Rosenkrantz et al., 2013) and (v2) (Weinreb et al., 2016; Vargas et al., 2016) were created in part to standardise the process of assessment and reporting of prostate mpMR, to improve agreement between radiologists with a detailed scoring criterion for individual mpMR modalities and overall. According to the five-point PI-RADS, the dominant modality for peripheral zone (PZ) lesions is the DWI, but the DCE modality can upgrade scores of 3 to 4. Whilst for

transitional zone (TZ) lesions, the overall assessment largely follows the T2W score, but lesions scored 2, and 3 can be upgraded to 3 and 4, respectively if DWI modality suggests two points greater than DWI (Weinreb et al., 2016; Vargas et al., 2016), as illustrated in Fig. 1 (left).

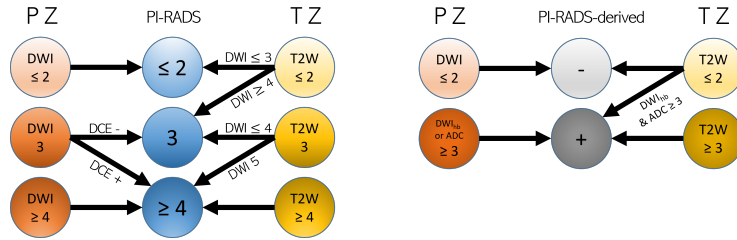


Figure 1: The illustration of PI-RADS v2 scoring system using a scale of 1-5 (left) and an example of the derived binary classification system used in this study (right).

Reporting mpMR images by radiologists is a labour-intensive task, and (Girometti et al., 2019) found substantial observer variance in assigning the PI-RADS v2 categories and assessing the spectrum of cancers found on whole-mount histology. Much of the literature (Litjens et al., 2014; Schelb et al., 2019; Chen et al., 2020; Hambarde et al., 2020; Chiou et al., 2020; Qian et al., 2021) has demonstrated that machine learning approaches, including deep learning, are potentially valuable tools that can help radiologists as first- and second assisting reader. Existing machine learning methods have exploited radiology knowledge to improve either classification or segmentation accuracy, including utilising prior knowledge of different lesion types in prostate zonal anatomy (Giannini et al., 2015; Duran et al., 2020; Van Sloun et al., 2021) and image modalities (De Vente et al., 2020; Chiou et al., 2020; Bonekamp et al., 2018) from available MR modalities <sup>1</sup>.

This paper investigates a different set of questions: a) whether summary information obtained from individual image modalities, such as “positive on T2W” or “anterior lesion on ADC” commonly reported in clinical practice, can first be predicted by deep learning models, before subsequent analysis? and b) how and whether this image

<sup>1</sup>In this work, an image modality is referred to a 3D image volume that observers commonly visualise, such as T2W, ADC, DWI<sub>hb</sub> or DCE, rather than individual MR modalities.

modality-independent representation can achieve adequate model performance, compared to the above end-to-end representation learning approaches, but for better model interpretation and feedback, which may lead to an eventual model improvement? These questions are interesting because the ability to quantify the importance, contribution and necessity of individual image modalities to the final prediction, provides a form of interpretation at the image modality level. This paper discusses specific clinical applications enabled by this individual modality quantification, in Sec. 3, which is also related to the literature discussing interpretable machine learning, further discussed in Sec. 4.

#### *Combining as late as possible, with hyperparameters*

Machine learning models can use a single image modality as input to ensure their predictions are independent of other image modalities. This independence reflects what is commonly applied in the clinical practice, in which radiologists often can localise and grade individual lesions on a single type of image before combining them for final reporting. The decision process of combining these modality-independent predictions, e.g., lesion-level classification and voxel-level segmentation, can be modelled by machine learning models, including non-parametric forms such as averaging or majority voting.

It is worth highlighting that the most researched model combining methods in literature, such as ensemble and committees, aim to improve the combined model performance. The model combining methods, in turn, can be parameterised with learnable parameters in an end-to-end optimisation as latent variables, such as the mixing coefficients in mixture models and the posterior probabilities in Bayesian model averaging. Some relevant examples are included in Sec. 2.

In contrast, this work combines predictions using modelled decision processes that are “hyperparameter-ised”, in order to enable a set of interesting applications, including 1) assessing existing decision processes in combining image modalities, and 2) discovering new decision rules with varying practical constraints, such as missing modality or known low-quality or otherwise challenging image modalities. As illustrated by the graphical model in Fig. 2 (a)-(b), model (a) represents the hyperparameterised combin-

ing model, which is referred to as “combiner models” in this paper, while model (b) represents a combining methods that jointly optimise the representation of individual image modalities and the combining decision.

The alternative “early fusion”, as illustrated in Fig. 2 (c), could be used to assess individual types’ importance and availability, similar to the “late combiner” in Fig. 2 (a) and the “late fusion” in Fig. 2 (b). However, after the combining process, combining input before representation learning loses the direct influence on the final prediction due to the less interpretable “black-boxed” neural networks. It is the uncomplicated link from individual image representation to the final prediction in Fig. 2 (a) and (b), often via weighted sum or its generalisation, that has motivated and enabled these above-discussed applications.

This paper describes the development of the deep neural networks based on individual modalities of mpMR images, combined with hyperparameterised decision-making models, as shown in Fig. 2 (d) for the challenging prostate cancer segmentation. Two rule-combining methods are proposed to represent linear and nonlinear decision rules, using low dimensional hyperparameters.

In addition, a hypernetwork is also developed, as shown in Fig. 2 (e) with varying hyperparameter values in a single neural network, for improved practical and efficient use of the proposed combiner networks, including searching for optimum rules. When the hyperparameters are required to be adjusted for analysis purpose, as is the case in this study, hypernetwork enables hyperparameter-adjusting during inference, avoiding the need to train many models with different values separately. These hypernetworks are referred to as HyperCombiner networks in this work.

The main hypothesis investigated in this study is that, with the added rule modelling, lesions segmentation models can achieve a non-compromising performance but are more interpretable. A set of experimental results are presented based on clinical mpMR images from 850 prostate cancer patients and multiple radiologist reports obtained in five clinical studies.

This study then investigates the benefit in incorporating the rule modelling, which enables addressing the following specific questions, in Secs. 4 and 5.

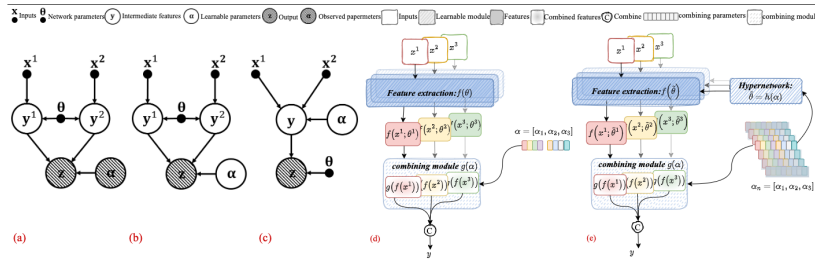


Figure 2: Graphical models from (a) to (c) use a single (shared) network with parameters  $\theta$ , where  $y^1$ ,  $y^2$  and  $y$  are intermediate features and  $\alpha$  is a set of parameters, to combine combining the inputs  $x^1$  and  $x^2$  and output  $z$ . (a) an example of late combiner models, of interest in this study, with observed  $\alpha$  in shaded circle, (b) late fusion in model combining methods with learnable  $\alpha$ , (c) an early fusion model for comparison. Hollow circles and solid dots indicate random variables and deterministic parameters, respectively. This is one example to show the difference between the combiner models (a) and other model combining methods (b and c), among other possible probabilistic graphical representations. Besides, (d) and (e) are respectively schematic diagram of the proposed Combiner and HyperCombiner, with three image modalities as example inputs.

- Does separating the representation for individual image modalities sacrifice the model performance, compared with an end-to-end learning?
- Are hypernetworks capable of summarising different hyperparameter values, representing different combining rules, in a single neural network?
- What is the impact for individual image modalities on the model performance, after adjusting hyperparameter values?
- Can the hyperparameters be optimised to obtain optimum decision rules via hyperparameter search?
- Are the empirical PI-RADS-derived rules better or worse than the above numerically optimised decision rules?
- Would any conclusion differ for tumours found in different prostate zones?

## 2. Related Work

### 2.1. Machine Learning for Prostate mpMR images

Recent studies have shown that mpMR images indicate clinically significant prostate cancer more than a single type of MR images (Chan et al., 2003; Haider et al., 2007).

Various methods have been proposed to detect and localise prostate lesions by extracting features from the mpMR images. Weak supervision or multiple instance learning methods using patient-level labels have also been investigated to avoid the need for lesion annotations (Mehta et al., 2021; Saha et al., 2021). Others learn such features using labels from radiologists or histopathology results, albeit the latter of which often are based on targeted biopsy (Litjens et al., 2014; Schelb et al., 2019; Chen et al., 2020; Mehralivand et al., 2022; Eidex et al., 2022). Cascaded lesion detection systems were proposed to extract a combination of radiology and anatomy features or regions from mpMR images and then classify or segment suspected candidates for cancerous likelihood. (Litjens et al., 2014) proposed two-stage networks, starting with initial candidates and then segmenting the candidates. The networks achieved patient-level ROC AUCs of 0.83 for clinically significant prostate cancer versus benign prostate cancer on a data cohort including 347 patients. (Mehralivand et al., 2022) presented automated detection and segmentation of prostate MRI lesions, followed by a 4-class classification task to predict PI-RADS categories 2 to 5. The experiments were conducted on 1043 MR scans and yielded 0.359 median DSC for lesion segmentation and 0.308 overall PI-RADS classification accuracy. (Eidex et al., 2022) proposed a cascaded scoring segmentation network consisting of region-of-interest localisation (ROI), identification of the object within the ROI, and definition of the target. The average centroid distance, volume difference, and DSC value for prostate/DIL obtained by networks were  $4.3 \pm 7.5/3.73 \pm 3.78$  mm,  $4.5 \pm 7.9/0.41 \pm 0.59$  cc, and  $0.896 \pm 0.089/0.843 \pm 0.119$ , respectively.

Others implemented end-to-end networks to segment suspected lesions using mpMR images (Chen et al., 2020; De Vente et al., 2020; Duran et al., 2020, 2022; Antonelli et al., 2019; Hambarde et al., 2020; Chiou et al., 2020; Qian et al., 2021; Woźnicki et al., 2020). (Chen et al., 2020) used multi-branched UNet to extract features from different modalities of MR image, achieving a Dice similarity coefficient (DSC) of 0.72 and a sensitivity of 0.74 at the 1.00 specificity. (De Vente et al., 2020) presented a method to segment prostate by encoding the Gleason Grade Group as ordinal classes of lesions, which scored a voxel-wise weighted kappa of  $0.446 \pm 0.082$  and a Dice similarity coefficient for clinically significant cancer segmenting  $0.370 \pm 0.046$ .

Prior knowledge of radiology, including clinical features and zonal prostate anatomy, is often used to improve the accuracy of lesion segmentation. (Duran et al., 2022) proposed an attention CNN for joint multi-class segmentation of prostate and cancer lesions by Gleason Score, which outperformed well-tuned U-Net, Attention U-Net, ENet and DeepLabv3+ at the task of detecting clinically significant prostate cancers. (Chiou et al., 2020) proposed a domain-adapted segmentation approach from routine mpMR images to VERDICT, a customised MR modality for prostate cancer, which yields substantial improvements without domain adaption.

In addition, literature has investigated the relationship between the radiologist’s assessment of PI-RADS and the algorithm’s automated assessment (Schelb et al., 2019; Youn et al., 2021; Wang et al., 2017; Sanford et al., 2020). (Wang et al., 2017) verified in 54 study cohorts that machine learning could improve the performance of PI-RADS assessment. (Youn et al., 2021) conducted experiments on datasets including patients who underwent pre-biopsy MRI and prostate biopsy to compare lesion detection and PI-RADS classification performance between U-Net, clinical reports and radiologists. The results showed that algorithms achieved moderate diagnostic performance with experts in PI-RADS and were similar to clinical reports from various radiologists in clinical practice.

Over the last few years, much work has been published to address the problem of prostate cancer localisation on mpMR images using machine learning-based methods, although little has addressed the image modality-related questions posed at the end of Sec. 1.

## 2.2. *Model Combining*

In literature, *model combining* refers to mixing or fusing individual branches as an ensemble output, usually purposed to improve the performance of the combined model and widely used in medical imaging tasks. Although they have a different aim from the *combiner* models of interest in this work, discussed in Sec. 1, many methodologies can be shared between the two.

(Greenspan et al., 2006) presented an unsupervised Gaussian mixture model (GMM)-based segmentation method for tissue classification of MR images of the brain. (Hassan



et al., 2019) also proposed an approach that employed fuzzy intelligence and GMM to detect carotid artery plaque in ultrasound images with high precision and strong robustness to noise. (Nguyen and Wu, 2012) proposed Markov random field with GMM that directly applied the EM algorithm to optimise the model parameters.

The two terms, early fusion and late fusion, are largely used in model combining, e.g. for multi-modality data input (D’mello and Kory, 2015; Snoek et al., 2005; Bi et al., 2022). As illustrated in Figs. 2 and discussed in Sec. 1, the late combiner developed in this work is conceptually close to the late fusion (Albashish et al., 2015; Wang et al., 2021b; Ghoniem et al., 2021; Boulahia et al., 2021; Mehta et al., 2021). (Albashish et al., 2015) proposed a prostate cancer diagnosis method that fused the probabilities outputs from the support vector machine and recursive feature elimination classifiers by a summary rule. (Wang et al., 2021b) proposed a fusion method for lung cancer survival analysis that exploited the correlations among predictions produced by different modalities regarding the model uncertainty and fused them by a weighted average scheme. (Ghoniem et al., 2021) developed a multi-modal fusion framework for ovarian cancer diagnosis, implementing CNN and LSTM as the base classifiers and weighted summation of the classification outputs with optimising hyperparameters. (Trong et al., 2020) developed a classification approach for weeds classification by using the late fusion of multi-modal deep neural networks via a voting method.

The works mentioned above combine base learners’ scores by applying fusion rules, such as voting, averaging and summation, while others search for deep fusion methods based on optimised strategies. (Boulahia et al., 2021) designed an end-to-end late fusion network where a deep neural network computes the merging score for action recognition. (Mehta et al., 2021) utilised a two-level support vector machine (SVM) to fuse the patient probability of prostate cancer predicted from mpMR features and clinical features. These kinds of fusion methods are also referred to as stacking ensemble learning (Ayache et al., 2007), which uses a meta-learner to combine the predictions of base learners (Wolpert, 1992). (Książek et al., 2020) proposed a stacking learning (ensemble) method to detect hepatocellular carcinoma, using SVM classifier to fuse seven base classifiers, including K-nearest neighbour, random forest, and Naïve Bayes. (Taspinar et al., 2021) used three single base learners, including the SVM, logistics

regression, and artificial neural network models, to produce classification probabilities and fuse them by a stacking meta-model to classify a total of 3486 chest X-ray images into three classes. (Wang et al., 2019) utilised a random forest classifier-based stacking technique to simultaneously construct the diagnostic model and combine them by decision tree for prostate cancer detection. (Saha et al., 2021) used a decision fusion model to ensemble the patch-based and image-based prediction by SVM classifiers to reduce false positives on prostate lesion segmentation.

In summary, these methods have been proposed to improve generalisation based on data from multiple modalities or models/methods, with promising results. They demonstrated that such human-adopted practice in combining data- or method-diverged decisions might be advantageous in practical applications, often constrained by data and other resources, over the alternative end-to-end black-box representation learning. However, we argue that the focus on performance represents a lost opportunity to utilise their simplicity and interpretability in these model combining methods, which have been evident with a lack of methodology and specific applications in using the so-called “interpretability”.

### 2.3. Hypernetworks

Deep learning methods strongly depend on tuning hyperparameters, such as the weights of the regularisation terms that can significantly affect the performance. Therefore, such hyperparameters must be carefully tuned to achieve the best result, which requires considerable time and computing resources. To address this issue, hypernetworks are proposed to train neural networks automatically adapted by various hyperparameters by re-parameterising the main network as a function of the hyperparameters, using a small auxiliary network (Ha et al., 2016; Lorraine and Duvenaud, 2018a) gave a theoretical justification for hypernetworks and used a gradient-based optimisation to tune hyperparameters. In hypernetwork training, weights of task network are regarded as a function of hyperparameters in loss functions or other hyperparameters of the task network itself. (Wang et al., 2021a) proposed a regularisation-independent reconstruction network, whose parameters are generated by a hypernetwork as a function of regularisation weights. (Hoopes et al., 2021) proposed a learning-based strategy for

deformable image registration, which replaces the tedious process of tuning important registration hyperparameters during training. (Ma et al., 2021) proposed a hyperconvolution layer which implicitly represents the convolution kernel as a function of “kernel coordinates”, led to improved accuracy.

Besides, others use hypernetwork training to adapt to multiple tasks using only a single hypernetwork. (Brock et al., 2017) accelerated the training procedure by learning an auxiliary hypernetwork that generates the weights of the main model for various architectures at the cost of a single training session. (Klocek et al., 2019) constructed an image representation network that takes an input image and returns weights to the target network to map points from the plane into their corresponding colours in the image.

Despite the promising studies mentioned above, hypernetworks have rarely been used to explain the “black box” of neural networks, which remains a worthwhile topic to be explored.

### 3. Method

#### 3.1. Image Modality-Independent Base Networks

Let us consider a problem to segment regions of interest from  $\tau$  types of images  $\mathbf{X}^\tau$  for each subject <sup>2</sup>. The segmentation using individual image modalities can be formulated as a voxel classification, such that each voxel  $i, i = 1, \dots, I$  is classified as either lesion or non-lesion voxel, where  $I$  is the number of voxels in each image. We would like to train a neural network  $f^\tau$  with a set of parameters  $\theta^\tau$  for each image modality  $\tau$  to predict the class probabilities  $\mathbf{Y}^\tau = [Y_1^\tau, \dots, Y_I^\tau]^\top, Y_i^\tau \in [0, 1], \tau = 1, \dots, \tau$ :

$$\mathbf{Y}^\tau = f^\tau(\mathbf{X}^\tau; \theta^\tau) \quad (1)$$

Given labelled training images  $\mathbf{x}_j^\tau = [x_{1,j}^\tau, \dots, x_{i,j}^\tau]^\top$  from  $J$  subjects, the networks  $f^\tau$  can be trained independently by minimising a segmentation loss  $\mathcal{L}$  between the predicted class probabilities  $\mathbf{y}_j^\tau = [y_{1,j}^\tau, \dots, y_{i,j}^\tau]^\top$  and the subject-specific labels  $\mathbf{t}_j =$

---

<sup>2</sup>Uppercase letters X, Y, Z and C denote random variables (if in bold, random vectors), with the corresponding lowercase letters are the observed scalars and vectors.

$[t_{1,j}, \dots, t_{i,j}]^T$ , i.e., the ground-truth segmentation masks available for individual subjects, where  $j = 1, \dots, J$ .

$$\hat{\theta}^\tau = \arg \min_{\theta} \sum_{j=1}^J \mathcal{L}(\mathbf{y}_j^\tau, \mathbf{t}_j) \quad (2)$$

where  $\mathbf{y}_j^\tau = f^\tau(\mathbf{x}_j^\tau; \theta^\tau)$  and  $\hat{\theta}^\tau$  is the set of optimised network parameters.

In our application, we consider a binary classification denoting all identified lesions as positive with  $\tau = 3$  types of images,  $y_i^\tau = \{0, 1\}$  and  $\tau = 1, 2, 3$  for respective T2W, DWI<sub>hb</sub> and ADC images. The formulation described here may be generalised to multi-class classification and more image types when, for example, detailed radiological/histopathological grading such as the five-point PI-RADS scores and other image modalities including DCE are available. A naturally extendable combination of cross-entropy and a soft Dice loss is used in this study.

$$\mathcal{L}(\mathbf{y}_j^\tau, \mathbf{t}_j) = \sum_{i=1}^I [t_{i,j} \log y_{i,j}^\tau + (1 - t_{i,j}) \log (1 - y_{i,j}^\tau)] - \frac{2 \sum_{i=1}^I (y_{i,j}^\tau \cdot t_{i,j}^\tau)}{\sum_{i=1}^I y_{i,j}^\tau + \sum_{i=1}^I t_{i,j}^\tau} \quad (3)$$

These image modality-specific networks are hereinafter referred to as ‘‘Base networks’’.

### 3.2. Modelling Rules to Combine: Combiner Networks

With the image modality-independent predictions  $\mathbf{Y}^\tau$  with the now shared  $\theta$  represents the feature extractor in the ‘‘Combiner network’’:

$$\mathbf{Y}^\tau = f(\mathbf{X}^\tau; \theta). \quad (4)$$

this section describes how these predictions can be combined to a ‘‘consensus’’ segmentation for each subject, as shown in Fig.3 (left). We share weights  $\theta$  among feature extractor  $f(\mathbf{X}^\tau; \theta)$  in Combiner with respect to three modalities of image, because a shared network may benefit from the multi-task effect, where different tasks regularize each other. However, separately trained networks may also be sufficient in this application, though this may require further investigation.

We propose two parametric functions, a linear mixture model and a nonlinear stacking model, before describing how these two functions can themselves be optimised and used to combine the base segmentation networks.

These proposed methods are closely related to several machine learning techniques, such as stacking ensemble (Wang et al., 2019), gating (Zhou et al., 2020) and late fusion in multi-task learning (Wang et al., 2021b), which are discussed further in Sec. 6.

### 3.2.1. Linear mixture model

The linear model  $g^{lin}$  is a weighted sum of predictions over all image modalities, therefore a voxel-wise function of  $\mathcal{Y} = [\mathbf{Y}^1, \dots, \mathbf{Y}^\tau]$ :

$$Z = g^{lin}(\mathcal{Y}; \boldsymbol{\alpha}) = \sum_{\tau=1}^{\tau} \alpha_{\tau} \cdot \mathbf{Y}^{\tau} = \sum_{\tau=1}^{\tau} \alpha_{\tau} \cdot f(\mathbf{X}^{\tau}; \boldsymbol{\theta}) \quad (5)$$

where  $\boldsymbol{\alpha} = [\alpha_1, \dots, \alpha_{\tau}]^{\top}$ ,  $\alpha_{\tau} \in [0, 1]$  and  $\sum_{\tau=1}^{\tau} \alpha_{\tau} = 1$  is a set of ‘‘mixing parameters’’, as in a mixture model. Recall that image modality-specific class probability  $Y_i^{\tau}$  represents a conditional probability given the image modality  $p(C | \tau)$ , where  $Y_i^{\tau} = p(C | \tau)$ . Thus, the mixture model represents a joint probability over all possible image modalities,  $Z_i = p(C) = \sum_{\tau=1}^{\tau} p(\tau)p(C | \tau)$ , where  $C$  denotes the class(es) of interest and  $p(\tau) = \alpha_{\tau}$ .

### 3.2.2. Nonlinear stacking model

Combining the predictions using a nonlinear function may also be useful. For example, the maximum function representing majority voting can be approximated by a sigmoid function or its variants. This section describes a generalisation to the above linear mixture model allowing such a nonlinear combination of class probabilities, such that:

$$Z = g^{nonl}(\mathcal{Y}; \boldsymbol{\beta}) = \sigma\left(\sum_{\tau=1}^{\tau} \beta_{\tau} \cdot \mathbf{Y}^{\tau} + \beta_0\right) = \sigma\left[\sum_{\tau=1}^{\tau} \beta_{\tau} \cdot f(\mathbf{X}^{\tau}; \boldsymbol{\theta}) + \beta_0\right] \quad (6)$$

where  $\boldsymbol{\beta} = [\beta_0, \beta_1, \dots, \beta_{\tau}]^{\top}$  is a set of ‘‘stacking parameters’’ and  $\beta_0$  is the bias term. For binary classification in this study, the logistic sigmoid function  $\sigma(a) = (1 + e^{-a})^{-1}$  is used to represent class probability  $Z_i = p(C) \in [0, 1]$ . This alternative nonlinear stacking function approximates the integral of  $p(C | \tau)$ , over all images types  $\tau$ , to obtain the marginalised class probability  $p(C) = \int_{\tau} p(C | \tau) \cdot d\tau$ . Although the mixture

model can be considered as a special case of this more general stacking formulation, these two terms are distinguished in the paper for clarity.

### 3.2.3. Training hyperparameterised Combiner networks

This section describes the segmentation network that can utilise all images types, as opposed to the Base networks. This single network can be trained using either the mixing parameters  $\alpha$  or the stacking parameters  $\beta$  as the *network hyperparameters*.

Now, given all  $\tau$  types of images  $\mathbf{x}_j^{\tau}$  and labels  $\mathbf{t}_j$  for each of the available training  $J$  subjects, as in Sec. 3.1, the network can be optimised by minimising the same loss as in Eq. 3:

$$\hat{\theta} = \arg \min_{\theta} \sum_{j=1}^J \mathcal{L}(\mathbf{z}_j, \mathbf{t}_j) \quad (7)$$

where  $\mathbf{z}_j = [z_{i,j}, \dots, z_{i,j}]^{\top}$  and  $z_{i,j}$  can be obtained through either  $g^{lin}([y_{i,j}^1, \dots, y_{i,j}^{\tau}]^{\top}; \alpha)$  or  $g^{nonl}([y_{i,j}^1, \dots, y_{i,j}^{\tau}]^{\top}; \beta)$  in Eq. 5 or Eq. 6, respectively.  $\theta$  is a set of network parameters that are no longer specific to any image modality, neither is the optimal  $\hat{\theta}$ .

It is worth noting here that, if  $\alpha$  or  $\beta$  were to be trained simultaneously with the shared network parameters  $\theta$ , they are no longer hyperparameters. As discussed in Sec. 1, previous work has suggested that a conceptually similar multi-branch formulation may provide potential performance benefits, through architectural constraints or additional image modality-specific supervision. However, these methods that are promising for improving generalisation are considered beyond the focus of this work and are not discussed further.

### 3.3. HyperCombiner Networks

This section introduces an additional hypernetwork, such that a single trained segmentation network can be conditioned on varying hyperparameters during inference, instead of training individual networks for each different set of hyperparameter values, as shown in Fig. 3 (right).

Let a hypernetwork module be a parametric function of a set of hyperparameters, e.g.,  $\alpha$ :

$$\tilde{\theta} = h(\alpha; \phi) \quad (8)$$

where  $\Phi$  is a set of hypernetwork parameters. The hypernetwork module generates the segmentation network parameters  $\tilde{\Theta}$ , such that the segmentation network parameters become a function of, and completely dependent on, 1) the input hyperparameter values  $\alpha$  and 2) the hypernetwork parameters  $\Phi$ . By re-parameterising the Combiner network in Eq. 4, the proposed segmentation network, equipped with the hypernetwork module, is referred to as the ‘‘HyperCombiner network’’:

$$\mathbf{Y}^\tau = f(\mathbf{X}^\tau; h(\tilde{\alpha}; \Phi)) \quad (9)$$

where  $\Phi$  are the only trainable parameters, i.e., being updated by the gradients during the iterative backpropagation-based optimisation.

The linear mixture model in Eq. 5 with parameters  $\alpha$  is used here as an example and the combined class probabilities are

$$Z = g^{lin}(\mathcal{Y}; \alpha) = \sum_{\tau=1}^{\tau} \alpha_\tau \cdot \mathbf{Y}^\tau = \sum_{\tau=1}^{\tau} \alpha_\tau \cdot f(\mathbf{X}^\tau; h(\tilde{\alpha}; \Phi)) \quad (10)$$

, while the hyperparameter for the nonlinear stacking model (Eq. 6) with the hypernetwork predicting  $\tilde{\beta}$  is omitted here for brevity. Fig. 3 illustrates an overall schematic for this network.

With the same training data set described as in Sec. 3.1 and Sec. 3.2, training the hypernetwork-added segmentation network HyperCombiner thus becomes optimising the hypernetwork parameters  $\Phi$ :

$$\hat{\Phi} = \arg \min_{\Phi} \sum_{j=1}^J \mathcal{L}(\mathbf{z}_j, \mathbf{t}_j) \quad (11)$$

The hyperparameters are randomly sampled from ranges of application interest, during training the HyperCombiner.

### 3.4. Hyperparameter Estimation

The HyperCombiner networks require hyperparameter values during inference. For the prostate mpMR imaging application, two estimation methods are described in this section, one approximating existing rules, such as those derived from PI-RADS described in the following Sec. 3.4.1, the other searching for the optimal ones among all plausible candidate rules, described in Sec. 3.4.2.

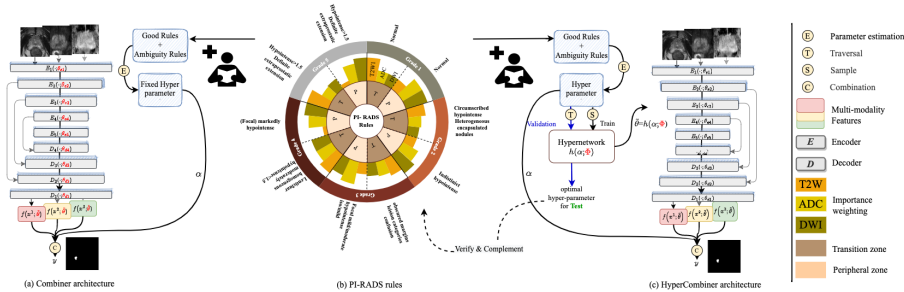


Figure 3: Illustration of the proposed Combiner (left) and HyperCombiner networks (right), which receive three types of images, T2W, DWI<sub>hb</sub> and ADC, as inputs. The hyperparameters  $\alpha$  are generated conditionally on certain combination parameters (b) and are used as combination parameters to combine the outputs of the three images in training. The parameters shown in red are the trainable weights of Combiner and HyperCombiner, respectively. All weights  $\theta$  in HyperCombiner are generated by an auxiliary hypernetwork  $\hat{\theta} = h(\alpha; \phi)$ .

Table 1: Example condition vectors and decisions for transition zone(TZ) lesions,  $\tau=1,2$  and 3 represent T2W, DWI<sub>hb</sub> and ADC, respectively. TZ denotes transition zone.

$C$	$p(C   \tau = 1)$	$p(C   \tau = 2)$	$p(C   \tau = 3)$	$p(C)$
TZ	negative	negative	negative	NEGATIVE
TZ	negative	negative	positive	NEGATIVE
TZ	negative	positive	negative	NEGATIVE
TZ	negative	positive	positive	POSITIVE
TZ	positive	negative	negative	POSITIVE
TZ	positive	negative	positive	POSITIVE
TZ	positive	positive	negative	POSITIVE
TZ	positive	positive	positive	POSITIVE

### 3.4.1. Encoding PI-RADS rules with condition and decision

As discussed in Sec. 1, radiological guideline scores individual image modalities, from different or the same MR modalities, then combine these scores with a set of rules.

For the purpose of this study, binary classification decisions, clinically significant or not, are determined by a set of rules on the three available image modalities, T2W, DWI<sub>hb</sub> and ADC, based on PI-RADS, as exemplified of transition zone in Table 1. Further discussion on the PI-RADS-derived rules for the transition- and peripheral lesions are provided in Appendix 2. In the experiments (Sec. 4), separate hyperparameters  $\hat{\alpha}^{(TZ)} / \hat{\beta}^{(TZ)}$  and  $\hat{\alpha}^{(PZ)} / \hat{\beta}^{(PZ)}$ , are specified for the lesions found in transition and peripheral zones, respectively, with their associated decisions  $d_k^{(TZ)}$  and  $d_k^{(PZ)}$ . The estimation methods are summarised in this section as follows.



*Condition vectors and associated decisions.* The PI-RADS rules can thus be encoded, with examples given in Table 1. Each row of  $P(C | \tau)$  represents a “condition vector”  $\mathbf{r}_k = [r_k^{\tau=1}, r_k^{\tau=2}, r_k^{\tau=3}]^\top, k = 1, \dots, K$  and  $r_k^\tau = \{0, 1\}$  (here,  $r_k^\tau = 0$  represents that modality  $\tau$  shows negative lesion and vice versa). There are a maximum of  $K = 2^3$  unique combinations of possible deterministic conditions  $\mathbf{r}_k$  and each of them has one associated “decision”  $d_k = \{0, 1\}$  (here,  $d_k = 0$  indicates that the final decision of the combined three modalities for the suspected lesion is negative, and vice versa) to indicate the joint binary probability for all image modalities. That is,

$$\mathbf{R} = \begin{bmatrix} 0 & 0 & 0 & 0 & 1 & 1 & 1 & 1 \\ 0 & 0 & 1 & 1 & 0 & 0 & 1 & 1 \\ 0 & 1 & 0 & 1 & 0 & 1 & 0 & 1 \end{bmatrix}, \mathbf{d} = \begin{bmatrix} 0 \\ 0 \\ 0 \\ 1 \\ 1 \\ 1 \\ 1 \\ 1 \end{bmatrix} \quad (12)$$

where  $\mathbf{R} = [\mathbf{r}_1, \dots, \mathbf{r}_K]$  and  $\mathbf{d} = [d_1, \dots, d_K]^\top$ .

*Estimation with linear decisions.* To estimate the hyperparameters  $\alpha_\tau$  with respect to the linear mixture model (Sec. 3.2.1) in Eq. 5, substitute random variables  $Y_i^\tau$  and  $Z_i$ , with  $r_k^\tau$  and  $d_k$ , respectively. The resulting linear system in matrix form is:

$$\mathbf{R}^\top \cdot \boldsymbol{\alpha} = \mathbf{d} \quad (13)$$

which can be solved by linear least-squares methods:

$$\hat{\boldsymbol{\alpha}} = \frac{(\mathbf{R}\mathbf{R}^\top)^{-1}\mathbf{R}\mathbf{d}}{\|(\mathbf{R}\mathbf{R}^\top)^{-1}\mathbf{R}\mathbf{d}\|_1} \quad (14)$$

This is equivalent to a *linear classification* problem, with the denominator to ensure that the mixing hyperparameters sum to one  $\sum_{\tau=1}^{\tau} \hat{\alpha}_\tau = 1$ .

*Estimation with nonlinear decisions.* The nonlinear stacking model (Sec. 3.2.2) can also be used, as an equivalent *logistic regression* problem. Substituting  $\mathbf{R}$  and  $\mathbf{d}$  into

Eq. 6, we have:

$$\sigma([\mathbf{R}^\top, \mathbf{1}] \cdot \boldsymbol{\beta}) = \mathbf{d} \quad (15)$$

where  $\mathbf{1}$  is vector of  $K$  ones and  $\sigma(\mathbf{a}) = [\sigma(a_0), \dots, \sigma(a_3)]^\top$  is the element-wise sigmoid function for a vector  $\mathbf{a} = [a_0, \dots, a_3]^\top$ . The estimated hyperparameter  $\hat{\boldsymbol{\beta}}$  can be obtained by iterative methods minimising the mean-square residuals:

$$\hat{\boldsymbol{\beta}} = \min_{\boldsymbol{\beta}} \|d - \sigma([\mathbf{R}^\top, \mathbf{1}] \cdot \boldsymbol{\beta})\|_2^2. \quad (16)$$

Both the linear and nonlinear hyperparameter estimation methods minimise the *a priori* risk in making wrong decisions from individual image modalities, as opposed to the empirical risk learned from data, which is discussed in the next section.

#### 3.4.2. Rule discovery as hyperparameter search

Using the encoded condition vectors in Table 1 may not be optimum, especially when the labels are not based on radiologist following these rules, such as Likert scores (Villers et al., 2006; Jung et al., 2004), or not rule-based at all, such as histopathological labels. Optimising the rules is equivalent to optimising the hyperparameters. Automated hyperparameter tuning has been an active research area for deep neural networks (Hoopes et al., 2021; Brock et al., 2017; Lorraine and Duvenaud, 2018b), and also a subject of the broad meta-learning study (Mantovani et al., 2015; Bui and Yi, 2020).

Using the proposed HyperCombiner, however, exhaustive search methods such as grid search becomes feasible, compared with the need to re-train the models for every sampled hyperparameter values. The trained HyperCombiner networks can be conditioned with different values sampled from each hyperparameter dimension of either the linear mixture models or the nonlinear stacking models during inference. In the following experiments and results, we also show the potentials in discovering new rules that may perform comparably or even better than those directly derived from PI-RADS using grid search strategy.

*Sampling for the linear mixture model.* The linear mixture model takes  $\boldsymbol{\alpha}$  as hyperparameters to combine the modality specific outputs as a final output. Here, in the training process, hyperparameters  $\boldsymbol{\alpha}$  are sampled from a Dirichlet distribution of  $\boldsymbol{\tau} = 3$

categories, which satisfies both constraints,  $\alpha_\tau \in [0, 1]$  and  $\sum_{\tau=1}^{\tau} \alpha_\tau = 1$ , defined in Sec. 3.2.1. During inference, samples are obtained with an equidistant interval of 0.1 in each hyperparameter dimension for a grid search.

*Sampling for the nonlinear stacking model.* Unlike linear mixture model, whose hyperparameters can be settled into Dirichlet’s space, the range of hyperparameters for non-linear stacking model is difficult to decide because of the logical functions involved. To investigate hyperparameters  $\beta$  that are corresponding to a set of interpretable rules, different combinations of decisions  $\mathbf{d}$  can be sampled. We used a one-layer logistic regression model to solve the Eq. (15). The regression fitting error,  $\|d - \sigma([\mathbf{R}^T, \mathbf{1}] \cdot \beta)\|_2^2$  as in Sec. 3.4.1, can be used to reject the implausible combinations. Details of acceptance-rejection of hyperparameters can be referred in Appendix 2.

### 3.4.3. Interpretation of the estimated hyperparameters

Here we describe three ways to understand then explain the estimated hyperparameter values, in turn, discuss the potential clinical applications of these interpretations.

*Quantifying necessity for image acquisition.* Several different image modalities have inter-dependence in their acquisition. For example, computing ADC may require both  $DWI_{hb}$  and DWI with low b values ( $DWI_{lb}$ ), but the  $DWI_{hb}$  and  $DWI_{lb}$  may be acquired independently without each other. These specialised imaging sequencing with practical constraints and variable feasibility is discussed further in Sec. 5 for specific clinical context. Setting one or more hyperparameters to zero(s), in Eqs. 5 and 6, allows the associated image modalities be omitted during inference. Therefore their respective added diagnostic values can be quantified by the difference in performance to the optimal values, using all available image modalities. When one or more image modalities are completely removed from prediction, the performance loss is quantified to investigate different data availability scenarios. It is essential to highlight that such necessity is quantified with respect to the use of machine learning models, which may differ from or sufficiently validate clinical practice where radiologists do not have access to such tools.

*Quantifying diagnostic importance of image modalities.* Linear decisions (Eq. 5) is a weighted sum of predictions from individual image modalities. Non-zero hyperparameter values  $\alpha$  can be used to compute the importance for each image modality, for example using the t-statistics (Molnar, 2020):

$$T_{\hat{\alpha}_\tau} = \frac{\hat{\alpha}_\tau - \alpha_\tau^0}{\mathbf{SE}(\hat{\alpha}_\tau)} \quad (17)$$

where  $\mathbf{SE}(\hat{\alpha}_\tau) = \sqrt{C_{\tau\tau}}$  is the standard error representing the variance of the individual linear regression coefficients, where  $C = \sigma_d^2(\mathbf{R}\mathbf{R}^\top)^{-1}$  is the variance-covariance matrix and  $\sigma_d^2$  is the decision variance; and,  $\alpha_\tau^0 = 0$  can be used to test the significance of image modalities, with other notations defined in Sec. 3.4. To quantify the relative importance between the  $\tau$  predictions,  $\alpha_\tau^0 = \frac{1}{\tau}$  can be used to represent equal contributions. This  $T_{\hat{\alpha}_\tau}$  directly measures how likely the combined decision will be changed due to the image modality  $\tau$ .

Using the nonlinear decision rules (Eq. 6), non-zero hyperparameter value  $\beta$  measures the log-ratio between the odds of the unit-incremented feature  $Y_i^\tau + 1$  and the estimated image modality-specific  $Y_i^\tau$ . Here, the odds of a specific image modality is the positive against negative probabilities  $odds(Y_i^\tau) = p(C = 1 | \tau) : p(C = 0 | \tau) = \frac{p(C=1|\tau)}{1-p(C=1|\tau)}$ , where  $Y_i^\tau = p(C | \tau)$ . In other words, the exponential of the estimated hyperparameter equals to the ratio of odds:

$$e^{\hat{\beta}_\tau} = \frac{odds(Y_i^\tau + 1)}{odds(Y_i^\tau)} \quad (18)$$

which indicates how much the image modality-specific influence is to the prediction.

In addition to the above general statistical interpretation, these estimated hyperparameters can be altered to assess their impact on metrics that are relevant to specific clinical applications, such as Type 1 and Type 2 errors for a downstream treatment decision following the machine learning-aided diagnosis or localisation. In this work, such sensitivity analysis was reported using the lesion-level recall and precision, designed for a class of tumour targeting applications that use the MR-derived lesion locations, described in Sec. 4.3.

*Quantifying uncertainty due to varying decision.* The proposed HyperCombiner networks enable efficient comparison between different decision rules during inference.

In addition to the optimum rule discovery described in Sec. 3.4.2, Monte-Carlo methods become feasible to estimate the variance of tumour localisation due to changing rules. This provides a means to quantify the type of uncertainty when image modality-related weightings can not be estimated or applied precisely, a common case in using and reading the clinical MR images of prostate cancer.

## 4. Experiment

### 4.1. Data sets

The mpMR images were acquired from 850 prostate cancer patients, which is from a part of several clinical trials conducted at University College London Hospital, including biopsy and treatment patient cohorts, including SmartTarget (Hamid et al., 2019), PICTURE (Simmons et al., 2018), ProRAFT (Orczyk et al., 2021), Index (Dickinson et al., 2013), PROMIS (Bosaily et al., 2015) and PROGENY (Linch et al., 2017). Of these, 651 patients had all three types of images, for a total of 751 combinations. All trial patients gave written consents and the ethics was approved as part of the respective trial protocols (Hamid et al., 2019). Radiologist contours were obtained for all lesions with Likert-scores  $\geq 3$  and served as ground-truth labels in this study. 22, 192, 325, 232 and 106 studies have 0, 1, 2, 3 and  $\geq 4$  lesions, respectively. There are 1962 lesion in total, out of which 207, 1443 and 312 lesions are located in peripheral zone, transition zone and across peripheral zone and transition zone. The original in plane dimension for T2W images ranges from  $180 \times 180$  to  $640 \times 640$  at resolution of  $1.31 \times 1.31 \text{mm}^2$  to  $0.29 \times 0.29 \text{mm}^2$ , respectively, and the thickness of T2W images ranges from 0.82 to 1mm. The original in plane dimension for DWI images ranges from  $96 \times 94$  to  $456 \times 320$  at resolution of  $3.41 \times 3.41 \text{mm}^2$  to  $0.75 \times 0.75 \text{mm}^2$ , respectively, and the thickness of DWI images ranges from 3 to 5 mm.

All the image modalities were resampled to isotropic-sized voxels  $1 \times 1 \times 1 \text{mm}^3$  with a linear interpolator and apply linear intensity normalization on per modality ranging from 0 to 1. The data set was divided into a training set, a validation set and a test set by patient, in a ratio of 4:1:1, so that one patient never appeared in a different data set.

## 4.2. Implementation

All the experiments were implemented with TensorFlow 2.4 and the networks were trained on an NVIDIA Tesla V100 GPU with 32 GB memory.

### 4.2.1. Multi-channel U-Net baseline networks

A U-Net segmentation network was implemented that takes concatenated three modality images as input to compare the modality-specific base network results with the modality-concatenated network. The modality-concatenated U-Net had the same structure as the Base network, except that there were three input channels.

### 4.2.2. Base networks

The base networks are built on the widely used U-Net (Ronneberger et al., 2015), which consists of an encoder-decoder with skip connections. The input to the base network was a batch of individual type images of size  $N \times 96 \times 96 \times 96 \times 1$ , where  $N$  is the batch size. A 3D convolutional layer was followed by Leaky Relu activation as the basic block in the encoder and decoder. The basic blocks had 16, 32, 32 and 32 channels in the encoder and 32, 32, 32, 32 and 16 channels in the decoder, where skip connections were used to build an information bridge between the encoder and decoder. We applied max-pooling with a factor of 2 after each basic block to reduce the spatial dimension four times in the encoder and then upsampled the feature maps of the basic blocks in the decoder until it reached the original input dimension. The last layer of the base network was a  $1 \times 1 \times 1$  convolutional layer followed by a sigmoid activation that generates a probability map representing the segmentation mask.

These three networks were separately trained with loss function Eq. (3) for 100 epochs using the ADAM optimizer with a learning rate of  $10^{-5}$ .

### 4.2.3. Combiner networks

The implementation of the Combiner networks is based on the Base networks, with an auxiliary combining module to combine the modality-independent output from three base networks. Three base networks share weights in this implementation. In this application, we use the fixed hyperparameters  $\alpha$  or  $\beta$  for training and testing, and the derived hyperparameters are stated in Sec. 5.1. The network is trained in with loss Eq. (3) using ADAM optimizer, with a learning rate equal to  $10^{-5}$ .

#### 4.2.4. HyperCombiner networks

The HyperCombiner network has the same structure as the Combiner network, implicitly representing the convolutional kernel as a function of hyperparameters by replacing the convolutional layer in Combiner with a hyperparameterized convolutional layer (Hoopes et al., 2021). The weights (and biases) of the Combiner network in this section are generated by an auxiliary hypernetwork, which, together with the combiner network itself is called the HyperCombiner network, as shown in Fig. 3 (right).

The hypernetwork consisted of 4 fully-connected layers, each with 64 units and followed by ReLU activation except for the final layer, which used Tanh activation. The hypernetwork provided all the weights and biases required in the Combiner network; therefore, only parameters in the hypernetwork became trainable.

*Train with linear mixture model.* The Combiner network of linear mixture model in HyperCombiner was the same as that of Combiner networks. During training, the hyperparameters were randomly sampled as described in Sec. 3.4.2. All HyperCombiner networks with linear mixture models have trained with the loss function in Eq. (3) for 100 epochs using the ADAM optimizer, with a learning rate of  $10^{-5}$ .

*Train with nonlinear stacking model.* The sampling was required from each iteration of training the HyperCombiner networks. To avoid cumbersome data transfer between the sample and neural network training, Algorithm 1 in Appendix 2 was run in advance for sufficient iterations and use these pre-computed hyperparameter values in neural network training.

Each network was trained for 400 iterations to converge using the ADAM optimizer with a  $10^{-5}$  learning rate.

### 4.3. Evaluation

All aforementioned experiments were tested with both voxel-level and lesion-level evaluation metrics.

#### 4.3.1. Voxel-level metrics

DSC and Hausdorff Distance (HD) are used as evaluation metrics at voxel-level. DSC measures the overlap between the predicted segmentation  $Y_p$  and the ground-

truth  $Y_g$ ,  $DSC = 2 \times |Y_p \cap Y_g| / (|Y_p| + |Y_g|)$ . HD measures the greatest surface distance between the boundaries of the predicted segmentation and the ground-truth. We report the 95<sup>th</sup> percentile of surface distances as a robust alternative, denoted as  $D_{HD}$ .

#### 4.3.2. Lesion-level metrics

The lesion-level evaluation metrics used in this study are adapted from those found in the object detection literature (Padilla et al., 2021), for our intended clinical targeting application, such as progression monitoring, targeted biopsy and focal therapy. Since multiple prostate lesions are often present in a single prostate MR image, directly applying object detection metrics has been found challenging in the application of multifocal cancers. In this study, we used modified asymmetric lesion-level evaluation metrics to evaluate the multifocal segmentation output, and further discussion of the motivation for these metrics is detailed in (Yan et al., 2022).

For each of  $N$  ground-truth lesions  $\{Y_g^n\}_{n=1,\dots,N}$ , it is considered as a true-positive lesion if it has overlap with any of the  $M$  predictions  $\{Y_p^m\}_{m=1,\dots,M}$ , single or multiple, that is greater than a pre-defined overlap threshold  $s^{GT}$ , otherwise false-negative. Thus,  $S^{GT} = \sum_{m=1}^M (Y_p^m \cap Y_g^n) / Y_g^n$ , with the superscripts  $GT$  indicating the ground-truth-based definitions, with which false-positive lesions is not defined. The recall thus can be computed as

$$recall^{GT} = TP^{GT} / (TP^{GT} + FN^{GT}), \quad (19)$$

where  $TP^{GT}$  and  $FN^{GT}$  are the numbers of true-positive and false-negative lesions using the ground-truth-based definitions, respectively.

For individual predicted lesions  $Y_p^m$ , a true-positive lesion requires the overlap with ground-truth regions  $Y_g^n$  to be greater than  $s^{Pred}$ , otherwise false-positive. Thus,  $S^{Pred} = \sum_{n=1}^N (Y_g^n \cap Y_p^m) / Y_p^m$ , with the superscripts  $Pred$  for the prediction-based definitions and undefined  $FN^{Pred}$ . Therefore,

$$precision^{Pred} = TP^{Pred} / (TP^{Pred} + FP^{Pred}). \quad (20)$$

When the cutoff value can be adapted in practice, the results of  $recall^{GT}$  with an equal  $precision^{Pred}=0.8$  (precision-controlled comparison of recall) and  $precision^{Pred}$



with an equal  $recall^{GT}=0.8$  (recall-controlled comparison of precision), denoted as  $recall^{*GT}$  and  $precision^{*Pred}$ , respectively, are also reported with their respective variable cutoff values.

#### 4.4. Comparison between Different Networks

We describe as follows a set of comparison experiments to demonstrate that a) the proposed HyperCombiner networks are capable of cancer segmentation, compared with the baseline networks, by testing several scenarios described as follows; and b) hyperparameters can be as conditioned accurately on the proposed HyperCombiner networks, compared with the individually trained Combiner networks.

##### 4.4.1. Using all three image modalities

Baseline performance of cancer segmentation is established using all image modalities available. The quantified performance between the baseline network (Sec. 4.2.1), Combiner networks and HyperCombiner, are compared when they are trained using all three available image modalities.

Four Combiner networks based on linear mixture models for two zonal lesions, each being trained with different decision values that represent 1) equally-weighted hyperparameters, and 2) PI-RADS-derived condition vectors. Two Combiner networks based on the nonlinear stacking models are trained with the PI-RADS-derived condition vectors. Two further HyperCombiner networks are trained and compared for the linear mixture- and the nonlinear stacking models, while the same set of decisions can be instantiated and tested during inference.

##### 4.4.2. Using individual image modalities

Combiner networks and HyperCombiner networks, when only individual image modalities are available, are compared with the prediction accuracy of the Base network with a single image modality. Here, the Combiner networks with single image modality input are considered baseline performance. These experiments provide a predictive reference performance concerning each image modality.

##### 4.4.3. Varying hyperparameter values

With two or more two types of images available, the difference in performance was also tested between the Combiner networks and HyperCombiner networks, with

varying hyperparameter values. Among possible permutations, setting individual hyperparameters to zero indicates predicting without using certain types of images. As described in the above section, predicting using individual image modalities is a special case when two of the hyperparameters are zero.

The permutation was possible during inference for HyperCombiner, while the Combiner models need to be trained separately for each set of hyperparameter values. The following were compared between the two networks, 1) PI-RADS-derived hyperparameters, described in Sec. 3.4.1, 2) the sampled hyperparameter values (including those being zeros), described in Sec. 3.4.2, and 3) for the linear mixture model-based networks, equal hyperparameters between all image modalities.

#### 4.5. Hyperparameter Analysis

This section describes experiments from the HyperCombiner networks, taking advantage of efficient conditioning of hyperparameter values.

Network performance using the metrics described in Sec. 4.3 was used for comparing different rules described below and, when applicable, statistics and a possible explanation of the hyperparameter values described in Sec. 3.4.3, are discussed.

##### 4.5.1. Comparing different rules

Different hyperparameter values, which were either derived from PI-RADS or randomly sampled as described in Sec. 4.4.3, were compared with the hyperparameter values with equal weights on all image modalities. The details of the used hyperparameter values are reported in Table 1 and Appendix 1.

##### 4.5.2. Rule discovery

The search for the optimum rule-defining hyperparameters was demonstrated with a grid search. The sampling of these parameters is described in Sec. 4.5. For the HyperCombiner with linear mixture models,  $\alpha$  was sampled between  $[0, 1]$  with equidistant intervals of 0.1. For the HyperCombiner with a nonlinear stacking model,  $\beta$  was first randomly sampled before being sorted for each hyperparameter for the grid search. Each possible combination of the hyperparameters  $\alpha_\tau$  and  $\beta_\tau$  was then tested, for computing the metrics defined in Sec. 4.3.

## 5. Results

### 5.1. PI-RADS-derived Decisions

Given a constant  $\mathbf{R}$  that contains all possible deterministic condition vectors, as in Eq. 12,  $\mathbf{d}^{(TZ)}$  and  $\mathbf{d}^{(PZ)}$  denote decisions for identifying lesions found in transition and peripheral zones, respectively. For comparison,  $\mathbf{d}^{(WG)}$  is also considered for lesions found in the whole gland regardless of their zonal location. Appendix 1 contains the details of obtaining these PI-RADS-derived decisions and the fitted hyperparameters.

Table 2: PI-RADS-derived decisions and the fitted hyperparameters, together with the corresponding residuals and importance-representing statistics (Sec. 3.4.3). The hyperparameters correspond to the three types of images in the same order of T2W,  $DWI_{hb}$  and ADC, following the optional bias  $\hat{\beta}_0$  in the nonlinear models<sup>4</sup>, for all the presented results.  $No. rule$  is the decimal value of decision vector  $\mathbf{d}$ .

Zones	$No. rule$	Decision $\mathbf{d}^T$	combining	Hyperparameters $\alpha(\beta)$	Residuals	Quantified diagnostic importance
WG	63	[0 0 1 1 1 1 1 1]	linear	$\hat{\alpha}^{(WG)} = [0.45, 0.45, 0.10]^T$	0.0781	$T_{\alpha} = [2.2048, 2.2048, 0.4410]$
			nonlinear	$\hat{\beta}^{(WG)} = [18.17, 18.17, -0.20, -8.53]^T$	$1.35 \times 10^{-7}$	$e^{\hat{\beta}} = [7.78 \times 10^7, 7.78 \times 10^7, 9.80 \times 10^{-1}, 1.97 \times 10^{-4}]$
TZ	31	[0 0 0 1 1 1 1 1]	linear	$\hat{\alpha}^{(TZ)} = [0.60, 0.20, 0.20]^T$	0.0625	$T_{\alpha} = [2.3664, 0.7888, 0.7888]$
			nonlinear	$\hat{\beta}^{(TZ)} = [30.67, 14.84, 14.84, -22.36]^T$	$1.77 \times 10^{-7}$	$e^{\hat{\beta}} = [2.09 \times 10^{13}, 2.79 \times 10^6, 2.79 \times 10^6, 1.95 \times 10^{-10}]$
PZ	119	[0 1 1 1 0 1 1 1]	linear	$\hat{\alpha}^{(PZ)} = [0.10, 0.45, 0.45]^T$	0.0781	$T_{\alpha} = [2.3094, 2.3094, 2.3094]$
			nonlinear	$\hat{\beta}^{(PZ)} = [-0.20, 18.17, 18.17, -8.53]^T$	$1.18 \times 10^{-6}$	$e^{\hat{\beta}} = [9.80 \times 10^{-1}, 7.78 \times 10^7, 7.78 \times 10^7, 1.97 \times 10^{-4}]$

As can be seen in Table 2, TZ lesions are more indicative with the T2W, although they require, like the PZ lesions, all three types of T2W,  $DWI_{hb}$  and ADC. This is consistent with the verbal description of the PI-RADS rules that determining positive lesions needs both T2W and DWI modalities. An interesting discussion between the requirement of either or both ADC and  $DWI_{hb}$  can be facilitated with their necessity analysis (Sec. 3.4.3), presented in Sec. 5.3.1.

### 5.2. Network Performance

The results in terms of network performance metrics, both voxel-level and lesion-level, are presented in Table 3, with their comparisons summarised in this section as follows.

#### 5.2.1. The Base networks

The base networks segmented cancers from each individual image modalities, with the  $DSC$  results ranging between [0.10, 0.12] in TZ and ranging between [0.27, 0.32] in PZ and the  $D_{HD}$  results that differed in their variances (i.e. St.D. range [9.2, 11.2])

<sup>4</sup> $\hat{\beta}$  is listed in order of  $[\beta_1, \beta_2, \beta_3, \beta_0]^T$  in all tables for readability, where the first three  $\beta$ s are ‘‘stacking parameters’’ in Eq.(15) and  $\beta_0$  is bias term.

Table 3: Summary of network performance. The first three rows are results of Base networks. The fourth row is results of the baseline network. From the fifth to eighth rows are the Combiner and HyperCombiner networks which are trained and tested with fixed PI-RADS-derived hyperparameters,  $\hat{\alpha}$  and  $\hat{\beta}$  in Table 1, for the linear and nonlinear models, respectively. The last rows show the best results of HyperCombiner’s hyperparameter search, which may differ for WG, TZ and PZ (see table 4 and 5 for details).

Methods	WG				TZ				PZ			
	<i>DSC</i>	<i>D<sub>HD</sub></i>	<i>Rec.*<sup>GT</sup></i>	<i>Prec.*<sup>pd</sup></i>	<i>DSC</i>	<i>D<sub>HD</sub></i>	<i>Rec.*<sup>GT</sup></i>	<i>Prec.*<sup>pd</sup></i>	<i>DSC</i>	<i>D<sub>HD</sub></i>	<i>Rec.*<sup>GT</sup></i>	<i>Prec.*<sup>pd</sup></i>
Base(T2W)	0.25(0.16)	17.55(9.65)	0.69	0.49	0.10(0.13)	24.09(13.11)	0.38	0.24	0.31(0.19)	17.72(10.33)	0.73	0.65
Base(DWI <sub>hb</sub> )	0.27(0.19)	<b>17.40</b> (11.17)	0.77	0.47	0.12(0.11)	24.35(13.80)	0.26	0.25	0.32(0.22)	17.18(10.77)	<b>0.75</b>	0.65
Base(ADC)	0.21(0.15)	17.75(9.18)	0.57	0.51	0.10(0.14)	23.45(11.86)	0.30	0.24	0.27(0.19)	18.37(10.33)	0.54	0.56
Baseline	0.31(0.18)	17.43(10.21)	0.72	0.61	0.13(0.10)	21.77(12.28)	0.45	0.31	0.35(0.21)	16.72(10.72)	0.66	0.66
Combiner <sup>(<math>\hat{\alpha}</math>)</sup>	0.29(0.17)	17.54(8.46)	0.68	<b>0.66</b>	0.12(0.11)	18.66(9.38)	0.47	0.33	0.33(0.20)	<b>16.22</b> (8.95)	0.73	0.69
Combiner <sup>(<math>\hat{\beta}</math>)</sup>	0.30(0.18)	17.57(8.25)	0.78	<b>0.66</b>	0.13(0.13)	<b>18.21</b> (8.59)	<b>0.64</b>	0.35	0.33(0.20)	17.46(9.35)	0.74	0.65
HypComb <sup>(<math>\hat{\alpha}</math>)</sup>	0.29(0.21)	17.71(9.62)	0.67	0.58	0.13(0.11)	19.52(7.55)	0.44	<b>0.37</b>	0.30(0.20)	17.16(9.26)	0.68	<b>0.73</b>
HypComb <sup>(<math>\hat{\beta}</math>)</sup>	0.31(0.20)	17.84(9.39)	0.79	0.46	0.11(0.18)	19.43(8.25)	0.55	0.26	0.33(0.19)	17.57(9.35)	0.67	0.64
HypComb <sup>(<math>\hat{\alpha}</math>)</sup>	<b>0.33</b> (0.22)	16.74(9.81)	0.47	0.51	<b>0.16</b> (0.08)	19.58(10.53)	0.48	0.22	0.36(0.24)	17.32(10.46)	0.66	0.50
HypComb <sup>(<math>\hat{\beta}</math>)</sup>	<b>0.33</b> (0.20)	<b>17.40</b> (9.65)	<b>0.81</b>	0.50	<b>0.16</b> (0.15)	18.81(8.99)	0.58	0.28	<b>0.37</b> (0.21)	16.90(9.23)	<b>0.75</b>	0.60

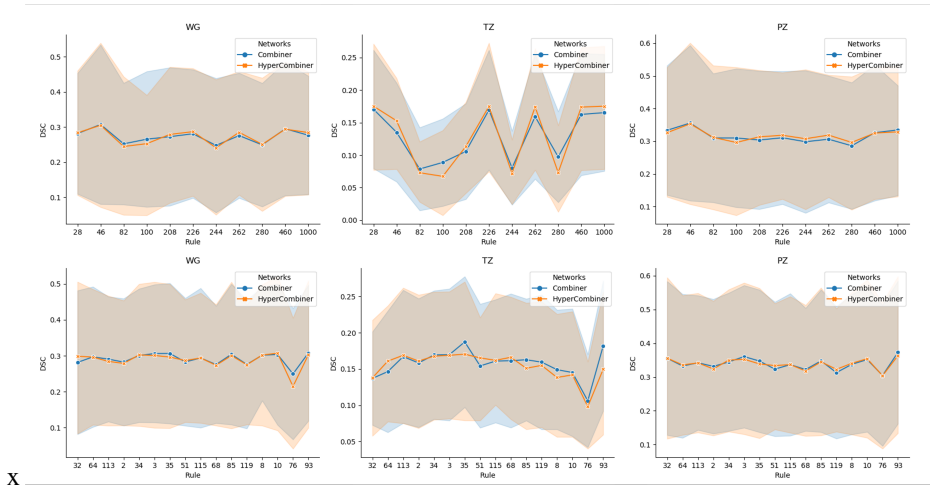
in WG).  $DWI_{hb}$  always gave the best results regardless of zones in which lesions were located. In terms of the lesion-level metrics,  $DWI_{hb}$  yielded the highest sensitivity ( $Recall*^{GT}=0.75$ ) in PZ, while T2W had the highest sensitivity ( $Recall*^{GT}=0.56$ ) among all three modalities in TZ. T2W and DWI have comparable positive predictive value  $Precision*^{pred}$  in both TZ and PZ.

### 5.2.2. Multi-channel U-Net baseline network

The baseline network achieved a  $DSC$  of  $0.31 \pm 0.18$  and a  $D_{HD}$  of  $17.43 \pm 10.21mm$  in the WG, together with its lesions-level accuracy for lesions found in different zones also provided in Table 3. These results provided a reference performance of a commonly-reported end-to-end cancer segmentation network. For lesions located in different regions of the gland, both voxel-level and lesion-level accuracy were higher than those of the Base network, except that  $Recall*^{GT}$  was slightly lower. This is also helpful evidence supporting the added diagnostic value of mpMR imaging, over individual image modalities, in the context of machine learning assistance.

### 5.2.3. The Combiner networks

Overall, the Combiner network trained with PI-RADS-derived hyperparameters in Table 3 achieved comparable results to the baseline network based on the performance of voxel and lesion levels in both TZ and PZ. Interestingly, despite the increased rule modeling ability of the linear stacking model, its overall predictive performance seems to observe a slight decline from lesions in the WG, with the  $DSC$  dropping from 0.35 to 0.33 (p-value = 0.002), suggesting that the rules derived from PI-RADS in the WG might be sub-optimal for linear mixture model.



X

Figure 4: The first and second row of figures compared the DSC between Combiner and HyperCombiner in terms of the linear mixture and nonlinear stacking models, respectively. Note that  $x$  coordinate was the  $No\_Rule$  of randomly selected combinations of hyperparameters.

#### 5.2.4. The HyperCombiner networks

The validity of the HyperCombiner networks is bench-marked by the segmentation metrics based on the Combiner networks for permuted hyperparameter values and different lesion locations, as shown in Fig. 4. The randomly selected ten combinations of hyperparameters were used to demonstrate the DSC values between the HyperCombiner and Combiner networks at the same hyperparameter values. The results showed that, in general, the single HyperCombiner networks are capable of replacing different Combiner networks trained with varying hyperparameter values.

### 5.3. Hyperparameter analysis and interpretation

#### 5.3.1. Image type availability of linear mixture model

Table 4 shows how the availability of image modalities affected the DSC of the linear mixture model by setting the corresponding hyperparameters of unavailable types to zeros.  $DWI_{hb}$  only and T2W only achieved the best performance in TZ and PZ, respectively. The Best results fro PZ and TZ were both yielded by T2W and  $DWI_{hb}$  combinations, albeit with different hyperparameters, suggesting that the combination of T2W and  $DWI_{hb}$  may be adequate without ADC.

It may be intuitive that the inferior lesion localisation ability from ADC may ad-

versely affect the overall performance in such an image modality-independent formulation, while it may not be the case for an end-to-end representation learning such as the baseline network.

Table 4: The results of HyperCombiner with linear mixture model that was evaluated under various fixed hyperparameters, and the three types of images are in the same order of (T2W,  $DWI_{hb}$ , ADC) for all the presented results. The last three rows showed the best rules that were ranked by grid searching on the validation set and tested on test set.

Hyperparameters - $\alpha$	WG				TZ				PZ				
	DSC	$D_{HD}$	$Rec.^{GT}$	$Prec.^{HD}$	DSC	$D_{HD}$	$Rec.^{GT}$	$Prec.^{HD}$	DSC	$D_{HD}$	$Rec.^{GT}$	$Prec.^{HD}$	
Single Image Type	[1,0,0]	0.30(0.21)	18.19(10.13)	0.55	0.37	0.12(0.12)	19.39(10.71)	0.34	0.10	0.34(0.23)	17.76(10.25)	0.67	0.48
	[0,1,0]	0.28(0.19)	19.10(9.91)	0.62	0.33	0.15(0.10)	19.53(9.85)	0.52	0.18	0.33(0.22)	18.73(10.07)	0.73	0.45
	[0,0,1]	0.23(0.18)	18.33(9.16)	0.35	0.29	0.10(0.13)	20.12(10.05)	0.25	0.13	0.27(0.20)	18.08(10.44)	0.50	0.41
Two Image Types	[0.5,0.5,0]	0.33(0.22)	16.74(9.81)	0.47	0.51	0.16(0.11)	19.20(10.43)	0.48	0.20	0.36(0.24)	17.32(10.46)	0.66	0.50
	[0,0.5,0.5]	0.28(0.20)	17.14(9.51)	0.63	0.42	0.14(0.15)	19.22(10.04)	0.20	0.23	0.31(0.22)	17.00(10.39)	0.71	0.49
	[0.5,0,0.5]	0.28(0.22)	17.20(10.00)	0.64	0.36	0.10(0.15)	22.36(12.78)	0.24	0.23	0.31(0.23)	17.62(11.01)	0.78	0.44
Equal Weights	$[\frac{1}{3}, \frac{1}{3}, \frac{1}{3}]$	0.30(0.20)	17.28(8.67)	0.68	0.44	0.13(0.12)	17.55(7.74)	0.54	0.19	0.33(0.22)	16.84(9.67)	0.63	0.49
Best for WG	[0.5,0.5,0.0]	0.33(0.22)	16.74(9.81)	0.47	0.51	/	/	/	/	/	/	/	/
Best for TZ	[0.4,0.6,0.0]	/	/	/	/	0.16(0.08)	19.58(10.53)	0.48	0.22	/	/	/	/
Best for PZ	[0.5,0.5,0.0]	/	/	/	/	/	/	/	/	0.36(0.24)	17.32(10.46)	0.66	0.50

### 5.3.2. Comparison of decision rules

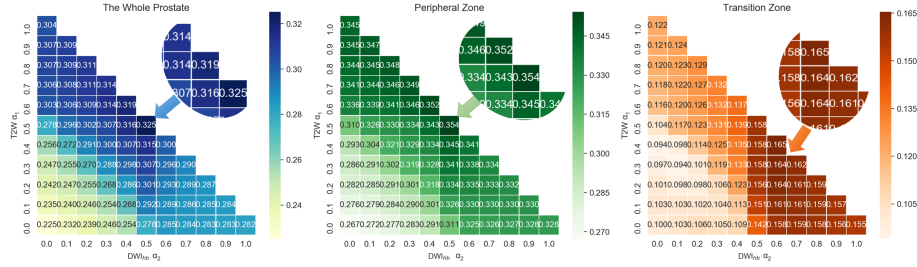


Figure 5: Grid search results on validation dataset of linear mixture learning heat map with various combinations of hyperparameters ( $\alpha_1, \alpha_2, \alpha_3$ ), where  $\alpha_1 + \alpha_2 + \alpha_3 = 1$ . Thus, we just show heat map of  $\alpha_1$  and  $\alpha_2$ , and corresponding  $\alpha_3 = 1 - \alpha_2 - \alpha_1$ .

*Results of linear decision rules.* Fig. 5 shows DSC accuracy of 55 linear rules using HyperCombiner in the grid search on validation dataset. The greater DSC values are found in the upper left-, upper right- and lower right parts of the triangle for the WG, PZ and TZ lesions, respectively. The observation implies that lesions in PZ and TZ were more accurately localised with more significant contributions from T2W and  $DWI_{hb}$ , respectively, compared to the lower left part of the triangle that represents the alternatively higher contribution from ADC. To a lesser degree, T2W was found to be more important than  $DWI_{hb}$  for PZ lesions and *vice versa* for TZ lesions. However, decreasing the weight on either  $DWI_{hb}$  or T2W lowered the DSC performance, generally consistent with the image availability analysis in Sec. 5.3.1.

More specifically, the best rules for linear mixture model were  $\alpha = [0.5, 0.5, 0]^T$  in the PZ, and  $\alpha = [0.4, 0.6, 0]^T$  in the TZ. What's more,  $\alpha = [0.5, 0.5, 0]^T$  produced the best results in WG as well, due to the size of the PZ being higher in the prostate than the TZ.

Table 5: Top five rules in terms of pixel-level evaluation metrics via grid search on the validation data of the non-linear stacking model, and tested on the test data. The  $No\_rule$  is decimal conversion of decision  $\mathbf{d}^T$ .

Zone	$No\_rule$	decisions $\mathbf{d}^T$								hyperparameters $\beta$				DSC	$D_{HD}$
WG	47	0	0	1	0	1	1	1	1	31.51	15.34	-15.49	-7.74	0.33(0.20)	17.40(8.92)
	63	0	0	1	1	1	1	1	1	18.17	18.17	-0.20	-8.53	0.31(0.20)	17.84(9.39)
	76	0	1	0	0	1	1	0	0	15.38	-31.55	15.38	-7.49	0.31(0.19)	18.24(8.46)
	43	0	0	1	0	1	0	1	1	17.53	17.53	-17.74	-8.58	0.31(0.21)	18.25(9.06)
	8	0	0	0	0	1	0	0	0	16.35	-16.74	-16.74	-8.52	0.31(0.18)	17.88(9.32)
TZ	32	0	0	1	0	0	0	0	0	-16.74	16.35	-16.74	-8.52	0.16(0.15)	18.81(8.99)
	48	0	0	1	1	0	0	0	0	-18.37	17.98	-0.21	-9.03	0.16(0.15)	18.58(8.67)
	34	0	0	1	0	0	0	1	0	-0.21	17.98	-18.37	-9.03	0.15(0.14)	19.11(9.21)
	63	0	0	1	1	1	1	1	1	18.17	18.17	-0.20	-8.53	0.15(0.16)	17.93(8.54)
	43	0	0	1	0	1	0	1	1	17.53	17.53	-17.74	-8.58	0.15(0.14)	18.51(9.01)
PZ	47	0	0	1	0	1	1	1	1	31.51	15.34	-15.49	-7.74	0.37(0.21)	16.90(9.23)
	63	0	0	1	1	1	1	1	1	18.17	18.17	-0.20	-8.53	0.35(0.23)	17.29(9.65)
	76	0	1	0	0	1	1	0	0	15.38	-31.55	15.38	-7.49	0.35(0.20)	17.70(8.79)
	8	0	0	0	0	1	0	0	0	16.35	-16.74	-16.74	-8.52	0.35(0.21)	17.44(9.37)
	15	0	0	0	0	1	1	1	1	19.94	-0.36	-0.36	-9.42	0.35(0.22)	17.52(9.32)

*Results of nonlinear decision rules.* Based on the test set, the top performing rules from the grid search are in Tables 5 and 6, ranked by the voxel-level and lesion-level accuracy, respectively. Rule 47 achieved the best DSC ( $0.37 \pm 0.21$ ) and  $D_{HD}$  ( $16.90 \pm 9.23mm$ ) for PZ lesions. Rule 32 and 63 achieved the best DSC ( $0.16 \pm 0.15$ ) and  $D_{HD}$  ( $17.93 \pm 8.54mm$ ) for TZ lesions, respectively. Investigating the hyperparameters sampled for the nonlinear decision rules (Sec. 3.4.2), which represent the odds-ratios for individual image modalities, the following conclusions were drawn, consistent with those from the linear models.

- The best lesion localisation results were achieved without ADC in terms of voxel-level results. This conclusion can be evident by Table 5 that 4, 5 and 4 out of the top five rules are fitted with decisions whose hyperparameters for ADC are negative values in WG, TZ and PZ, respectively. ADC was the least indicative of lesion localisation among the three image modalities.
- For a PZ lesion, according to voxel-level results in Table 5, all hyperparameters of the T2W modality are positive in the top five rules. Thus, a lesion was con-

sidered positive if it was found positive on T2W, regardless of any other image pattern. But their arguably marginal difference in voxel-level accuracy.

- The TZ lesions were considered positive if found positive on  $DWI_{hb}$ , without considering any other image modalities.
- In terms of lesion-level metrics,  $DWI_{hb}$  and ADC weighed more than T2W according to Table 6. The top three rules for  $Recall^{*GT}$  are largely achieved with positive hyperparameters of DWI, while the top three rules for  $Precision^{*Pred}$  had positive hyperparameters for  $DWI_{hb}$  and ADC images.

Table 6: Top three rules in terms of lesion-level evaluation metrics via grid search on the validation data of the non-linear stacking model, and tested on the test data. The  $No_{,rule}$  is decimal conversion of decisions  $\mathbf{d}$

Zone	Ranked by	$No_{,rule}$	decisions $\mathbf{d}^T$							hyperparameters $\beta$				$Rec_{,}^{*GT}$	$Prec_{,}^{*pd}$	AUC	
WG	Recall	43	0	0	1	0	1	0	1	1	17.53	17.53	-17.74	-8.58	0.82	0.55	0.67
		34	0	0	1	0	0	0	1	0	-0.21	17.98	-18.37	-9.03	0.82	0.56	0.69
		48	0	0	1	1	0	0	0	0	-18.37	17.98	-0.21	-9.03	0.81	0.56	0.68
	Precision	117	0	1	1	1	0	1	0	1	-15.49	15.34	31.51	-7.74	0.74	0.64	0.69
		19	0	0	0	1	0	0	1	1	14.23	29.15	14.23	-36.02	0.59	0.63	0.62
		17	0	0	0	1	0	0	0	1	-0.35	17.05	17.05	-25.57	0.74	0.62	0.67
	AUC	113	0	1	1	1	0	0	0	1	-17.74	17.53	17.53	-8.58	0.81	0.61	0.71
		117	0	1	1	1	0	1	0	1	-15.49	15.34	31.51	-7.74	0.74	0.64	0.69
		34	0	0	1	0	0	0	1	0	-0.21	17.98	-18.37	-9.03	0.82	0.56	0.69
TZ	Recall	47	0	0	1	0	1	1	1	31.51	15.34	-15.49	-7.74	0.62	0.28	0.41	
		48	0	0	1	1	0	0	0	0	-18.37	17.98	-0.21	-9.03	0.61	0.28	0.43
		34	0	0	1	0	0	0	1	0	-0.21	17.98	-18.37	-9.03	0.59	0.29	0.44
	Precision	19	0	0	0	1	0	0	1	1	14.23	29.15	14.23	-36.02	0.30	0.34	0.32
		1	0	0	0	0	0	0	0	1	14.74	14.74	14.74	-37.27	0.34	0.32	0.34
		49	0	0	1	1	0	0	0	1	-15.23	30.51	14.83	-22.59	0.40	0.32	0.37
	AUC	34	0	0	1	0	0	0	1	0	-0.21	17.98	-18.37	-9.03	0.59	0.29	0.44
		48	0	0	1	1	0	0	0	0	-18.37	17.98	-0.21	-9.03	0.61	0.28	0.43
		63	0	0	1	1	1	1	1	1	18.17	18.17	-0.20	-8.53	0.56	0.28	0.43
PZ	Recall	34	0	0	1	0	0	0	1	0	-0.21	17.98	-18.37	-9.03	0.76	0.64	0.69
		113	0	1	1	1	0	0	0	1	-17.74	17.53	17.53	-8.58	0.75	0.67	0.70
		63	0	0	1	1	1	1	1	1	18.17	18.17	-0.20	-8.53	0.73	0.59	0.67
	Precision	17	0	0	0	1	0	0	0	1	-0.35	17.05	17.05	-25.57	0.66	0.68	0.66
		113	0	1	1	1	0	0	0	1	-17.74	17.53	17.53	-8.58	0.75	0.67	0.70
		117	0	1	1	1	0	1	0	1	-15.49	15.34	31.51	-7.74	0.67	0.67	0.67
	AUC	113	0	1	1	1	0	0	0	1	-17.74	17.53	17.53	-8.58	0.75	0.67	0.70
		34	0	0	1	0	0	0	1	0	-0.21	17.98	-18.37	-9.03	0.76	0.64	0.69
		43	0	0	1	0	1	0	1	1	17.53	17.53	-17.74	-8.58	0.70	0.62	0.68

### 5.3.3. Clinical case studies

Fig. 6 shows two examples of test cases with segmentation results from different methods. Rule 63  $\mathbf{d} = [0, 0, 1, 1, 1, 1, 1, 1]^T$ , which emphasises T2W and ADC prediction during the combining model, yields a DSC of 0.41, which is comparable to the baseline method. In contrast, Rule 15, which emphasises only T2W in the combining model, has a much lower DSC than Rule 63. As we stated in the previous section,



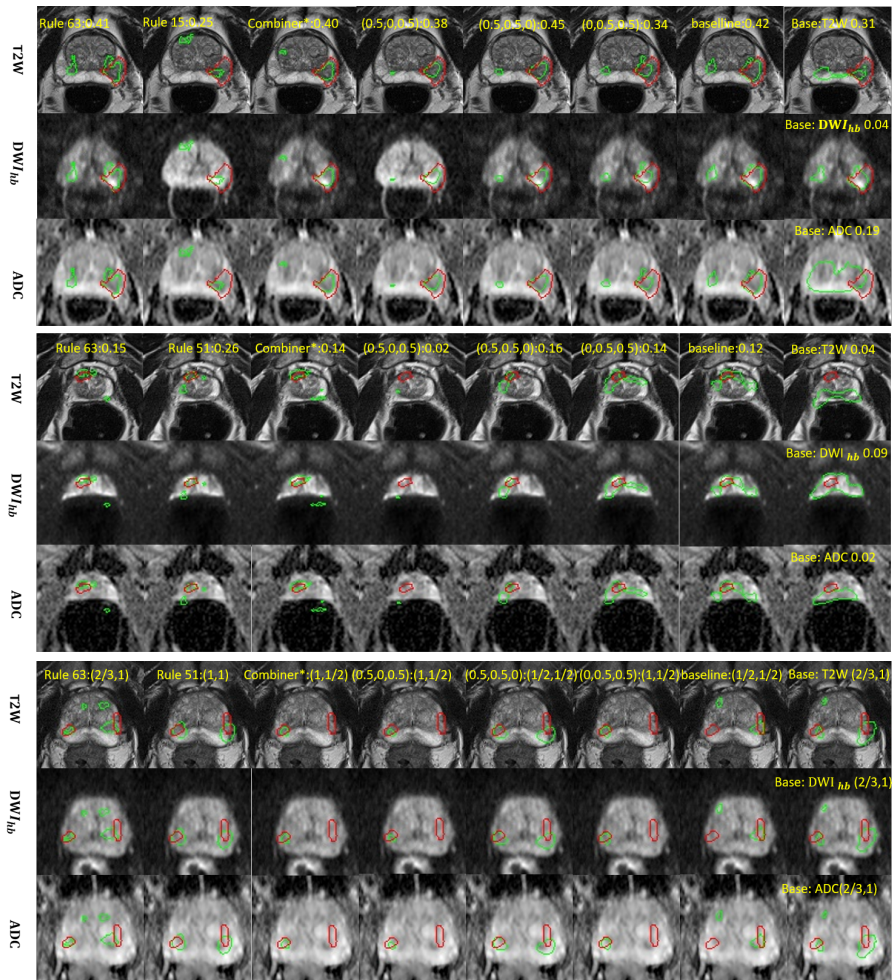


Figure 6: The results of nonlinear stacking, linear mixing, baseline models, and base networks are visualized from left to right, respectively. The first block and the second block show DSC results of peripheral zone lesion and transition zone lesion, respectively. The third block show the lesion-level results ( $Precision^{*Pred}$  and  $Recall^{*GT}$ , respectively) in the brackets.

the T2W+DWI<sub>hb</sub> combination improves the accuracy of lesion localisation. The third column is predicted by the non-linear stacking model of the Combiner model (denoted Combiner\*), which has a DSC comparable to Rule 63. It demonstrates the effectiveness of HyperCombiner’s ability to handle multiple hyperparameters.

In terms of the linear mixture model, the combination T2W+DWI<sub>hb</sub> produces the best DSC of 0.45. It is worth noting that the variation of results with different linear combinations is not as significant as the non-linear stacking model. The final column shows the results for the Base network, which is based on a single type of image for lesion segmentation, with DWI producing the best DSC, slightly slower than the baseline approach.

For TZ lesions from 4th to 6th rows, the non-linear stacking model with Rule 51  $\mathbf{d} = [0, 0, 1, 1, 0, 0, 1, 1]^T$ , emphasising DWI in the combined model, achieved the best DSC of 0.26 among all methods, much higher than the baseline method. In addition, the linear mixed model of T2W+ADC produced the worst segmentation mask compared to the other two combinations. By comparing the linear mixed model with the baseline network, we conclude that multiple types of images can be beneficial in the localisation of lesions.

## 6. Discussion

Common in clinical decision making, multiple sources are often combined to reach an informed consensus. Localising prostate cancer from multiple types of MR images is an example in uro-radiology. Many recently developed deep learning methods focus on exploiting the representation ability of neural networks without considering how different image modalities from multiple MR modalities are combined. This work investigates approaches which, without sacrificing any predictive ability of the segmentation model, model the combining process effectively and efficiently. The proposed Combiner and HyperCombiner networks bring explainable, quantitative decision making for different image types and how they are combined for the task.

The proposed approach allowed the comparison between different image modalities, whose availability associates with real-world cost and feasibility. As a result of this work, we have proposed decision rules that may be advantageous for emerging

machine learning models, but these may also be considered new potential protocols for further radiological practice. What is not included in this work is the ability to incorporate using the proposed method is known prior knowledge that is related to the importance of individual types, such as quantifiable quality of image quality (Saeed et al., 2022) and local expertise. For example, given a local estimate of below-average image quality and resonance time constraints, certain image modality may need to be weighed down to reach optimum tumour localisation performance.

Future work may consider multiple classes of the tumours, such as those based on the five-point PI-RADS scores. In addition to the intended radiology application, the provided analysis on the image modality availability may give urologists a good indication of the image modalities of most value when facing choices such as repeated biopsy, therapy options or surgery. This may also benefit from a system that is learned using the histopathology labels when they are available. However, developing better-than-radiologist machine learning models learned from histopathology labels remains an open research question.

More generally, the proposed approach opens an investigation between the so-called black-box approaches represented by deep learning and the classical decision rule modelling, arguably more challenging to optimise and generalise. In particular, biomedical imaging applications have seen an abundance of multimodal input tasks, and many could benefit from this hybrid machine learning framework.

The results presented in this work need to be interpreted with their limitations. For example, although this study used a relatively large data set from real clinical patients, the imaging and label data come from a single referral centre with significant experience in imaging and mpMR reading. Multi-centre research may be required to generalise specific clinical conclusions further. For example, the optimised rules may be subject to local protocols; therefore, they should consider further constraints or characteristics. When these conditions are identified, the proposed decision rule modelling approach should also be applicable.

## 7. Conclusion

PI-RADS rule has widely been used in lesion localisation by radiologists. Based on this rule, we proposed Combiner networks that use pre-defined decision rules to combine the modality-specific class probabilities with the linear mixture model and non-linear stacking model. Further development in the HyperCombiner networks enables more efficient hyperparameter analysis. The applications of the resulting Combiner and HyperCombiner networks are demonstrated using sizable clinical mpMR data set. We presented extensive experimental results to show a number of interesting comparisons between different image modalities and a potential to devise new and more effective rules to combine the modalities, under the specific clinical context of localising prostate cancer.

## Acknowledgment

This work was supported by the International Alliance for Cancer Early Detection, an alliance between Cancer Research UK [C28070/A30912; C73666/A31378], Canary Center at Stanford University, the University of Cambridge, OHSU Knight Cancer Institute, University College London and the University of Manchester. This work was also supported by the Wellcome/EPSRC Centre for Interventional and Surgical Sciences [203145Z/16/Z].

## References

- Ahmed, H.U., Bosaily, A.E.S., Brown, L.C., Gabe, R., Kaplan, R., Parmar, M.K., Collaco-Moraes, Y., Ward, K., Hindley, R.G., Freeman, A., et al., 2017. Diagnostic accuracy of multi-parametric mri and trus biopsy in prostate cancer (promis): a paired validating confirmatory study. *The Lancet* 389, 815–822.
- Albashish, D., Sahran, S., Abdullah, A., Adam, A., Abd Shukor, N., Pauzi, S.H.M., 2015. Multi-scoring feature selection method based on svm-rfe for prostate cancer diagnosis, in: 2015 International Conference on Electrical Engineering and Informatics (ICEEI), IEEE. pp. 682–686.

- Antonelli, M., Johnston, E.W., Dikaivos, N., Cheung, K.K., Sidhu, H.S., Appayya, M.B., Giganti, F., Simmons, L.A., Freeman, A., Allen, C., et al., 2019. Machine learning classifiers can predict gleason pattern 4 prostate cancer with greater accuracy than experienced radiologists. *European radiology* 29, 4754–4764.
- Ayache, S., Quénot, G., Gensel, J., 2007. Classifier fusion for svm-based multimedia semantic indexing, in: *European Conference on Information Retrieval*, Springer. pp. 494–504.
- Bi, L., Fulham, M., Kim, J., 2022. Hyper-fusion network for semi-automatic segmentation of skin lesions. *Medical Image Analysis* 76, 102334.
- Bonekamp, D., Kohl, S., Wiesenfarth, M., Schelb, P., Radtke, J.P., Götz, M., Kickingereder, P., Yaqubi, K., Hitthaler, B., Gähler, N., et al., 2018. Radiomic machine learning for characterization of prostate lesions with mri: comparison to adc values. *Radiology* 289, 128–137.
- Bosaily, A.E.S., Parker, C., Brown, L., Gabe, R., Hindley, R., Kaplan, R., Emberton, M., Ahmed, H., Group, P., et al., 2015. Promis—prostate mr imaging study: a paired validating cohort study evaluating the role of multi-parametric mri in men with clinical suspicion of prostate cancer. *Contemporary clinical trials* 42, 26–40.
- Bouahia, S.Y., Amamra, A., Madi, M.R., Daikh, S., 2021. Early, intermediate and late fusion strategies for robust deep learning-based multimodal action recognition. *Machine Vision and Applications* 32, 1–18.
- Brock, A., Lim, T., Ritchie, J.M., Weston, N., 2017. Smash: one-shot model architecture search through hypernetworks. *arXiv preprint arXiv:1708.05344* .
- Bui, K.H.N., Yi, H., 2020. Optimal hyperparameter tuning using meta-learning for big traffic datasets, in: *2020 IEEE International Conference on Big Data and Smart Computing (BigComp)*, IEEE. pp. 48–54.
- Chan, I., Wells III, W., Mulkern, R.V., Haker, S., Zhang, J., Zou, K.H., Maier, S.E., Tempany, C.M., 2003. Detection of prostate cancer by integration of line-scan dif-

- fusion, t2-mapping and t2-weighted magnetic resonance imaging; a multichannel statistical classifier. *Medical physics* 30, 2390–2398.
- Chen, Y., Xing, L., Yu, L., Bagshaw, H.P., Buyyounouski, M.K., Han, B., 2020. Automatic intraprostatic lesion segmentation in multiparametric magnetic resonance images with proposed multiple branch unet. *Medical physics* 47, 6421–6429.
- Chiou, E., Giganti, F., Punwani, S., Kokkinos, I., Panagiotaki, E., 2020. Harnessing uncertainty in domain adaptation for mri prostate lesion segmentation, in: *International Conference on Medical Image Computing and Computer-Assisted Intervention*, Springer. pp. 510–520.
- De Vente, C., Vos, P., Hosseinzadeh, M., Pluim, J., Veta, M., 2020. Deep learning regression for prostate cancer detection and grading in bi-parametric mri. *IEEE Transactions on Biomedical Engineering* 68, 374–383.
- Dickinson, L., Ahmed, H.U., Kirkham, A., Allen, C., Freeman, A., Barber, J., Hindley, R.G., Leslie, T., Ogden, C., Persad, R., et al., 2013. A multi-centre prospective development study evaluating focal therapy using high intensity focused ultrasound for localised prostate cancer: the index study. *Contemporary clinical trials* 36, 68–80.
- D’mello, S.K., Kory, J., 2015. A review and meta-analysis of multimodal affect detection systems. *ACM computing surveys (CSUR)* 47, 1–36.
- Duran, A., Dussert, G., Rouvière, O., Jaouen, T., Jodoin, P.M., Lartizien, C., 2022. Prostattention-net: A deep attention model for prostate cancer segmentation by aggressiveness in mri scans. *Medical Image Analysis* 77, 102347.
- Duran, A., Jodoin, P.M., Lartizien, C., 2020. Prostate cancer semantic segmentation by gleason score group in bi-parametric mri with self attention model on the peripheral zone, in: *Medical Imaging with Deep Learning*, PMLR. pp. 193–204.
- Eidex, Z.A., Wang, T., Lei, Y., Axente, M., Akin-Akintayo, O.O., Ojo, O.A.A., Akintayo, A.A., Roper, J., Bradley, J.D., Liu, T., et al., 2022. Mri-based prostate and

- dominant lesion segmentation using cascaded scoring convolutional neural network. *Medical Physics* .
- Ghoniem, R.M., Algarni, A.D., Refky, B., Ewees, A.A., 2021. Multi-modal evolutionary deep learning model for ovarian cancer diagnosis. *Symmetry* 13, 643.
- Giannini, V., Mazzetti, S., Vignati, A., Russo, F., Bollito, E., Porpiglia, F., Stasi, M., Regge, D., 2015. A fully automatic computer aided diagnosis system for peripheral zone prostate cancer detection using multi-parametric magnetic resonance imaging. *Computerized Medical Imaging and Graphics* 46, 219–226.
- Girometti, R., Giannarini, G., Greco, F., Isola, M., Cereser, L., Como, G., Sioletic, S., Pizzolitto, S., Crestani, A., Ficarra, V., et al., 2019. Interreader agreement of pi-rads v. 2 in assessing prostate cancer with multiparametric mri: A study using whole-mount histology as the standard of reference. *Journal of Magnetic Resonance Imaging* 49, 546–555.
- Greenspan, H., Ruf, A., Goldberger, J., 2006. Constrained gaussian mixture model framework for automatic segmentation of mr brain images. *IEEE transactions on medical imaging* 25, 1233–1245.
- Ha, D., Dai, A., Le, Q.V., 2016. Hypernetworks. *arXiv preprint arXiv:1609.09106* .
- Haider, M.A., Van Der Kwast, T.H., Tanguay, J., Evans, A.J., Hashmi, A.T., Lockwood, G., Trachtenberg, J., 2007. Combined t2-weighted and diffusion-weighted mri for localization of prostate cancer. *American journal of roentgenology* 189, 323–328.
- Hambarde, P., Talbar, S., Mahajan, A., Chavan, S., Thakur, M., Sable, N., 2020. Prostate lesion segmentation in mr images using radiomics based deeply supervised u-net. *Biocybernetics and Biomedical Engineering* 40, 1421–1435.
- Hamid, S., Donaldson, I.A., Hu, Y., Rodell, R., Villarini, B., Bonmati, E., Tranter, P., Punwani, S., Sidhu, H.S., Willis, S., et al., 2019. The smarttarget biopsy trial: a prospective, within-person randomised, blinded trial comparing the accuracy of visual-registration and magnetic resonance imaging/ultrasound image-fusion targeted biopsies for prostate cancer risk stratification. *European urology* 75, 733–740.

- Hassan, M., Murtza, I., Hira, A., Ali, S., Kifayat, K., 2019. Robust spatial fuzzy gmm based mri segmentation and carotid artery plaque detection in ultrasound images. *Computer methods and programs in biomedicine* 175, 179–192.
- Hoopes, A., Hoffmann, M., Fischl, B., Gutttag, J., Dalca, A.V., 2021. Hypermorph: Amortized hyperparameter learning for image registration, in: *International Conference on Information Processing in Medical Imaging*, Springer. pp. 3–17.
- Jung, J.A., Coakley, F.V., Vigneron, D.B., Swanson, M.G., Qayyum, A., Weinberg, V., Jones, K.D., Carroll, P.R., Kurhanewicz, J., 2004. Prostate depiction at endorectal mr spectroscopic imaging: investigation of a standardized evaluation system. *Radiology* 233, 701–708.
- Klocek, S., Maziarka, Ł., Wołczyk, M., Tabor, J., Nowak, J., Śmieja, M., 2019. Hypernetwork functional image representation, in: *International Conference on Artificial Neural Networks*, Springer. pp. 496–510.
- Książek, W., Hammad, M., Pławiak, P., Acharya, U.R., Tadeusiewicz, R., 2020. Development of novel ensemble model using stacking learning and evolutionary computation techniques for automated hepatocellular carcinoma detection. *Biocybernetics and Biomedical Engineering* 40, 1512–1524.
- Linch, M., Goh, G., Hiley, C., Shanmugabavan, Y., McGranahan, N., Rowan, A., Wong, Y., King, H., Furness, A., Freeman, A., et al., 2017. Intratumoural evolutionary landscape of high-risk prostate cancer: the progeny study of genomic and immune parameters. *Annals of Oncology* 28, 2472–2480.
- Litjens, G., Debats, O., Barentsz, J., Karssemeijer, N., Huisman, H., 2014. Computer-aided detection of prostate cancer in mri. *IEEE transactions on medical imaging* 33, 1083–1092.
- Lorraine, J., Duvenaud, D., 2018a. Stochastic hyperparameter optimization through hypernetworks. CoRR abs/1802.09419. URL: <http://arxiv.org/abs/1802.09419>, arXiv:1802.09419.



- Lorraine, J., Duvenaud, D., 2018b. Stochastic hyperparameter optimization through hypernetworks. arXiv preprint arXiv:1802.09419 .
- Ma, T., Dalca, A.V., Sabuncu, M.R., 2021. Hyper-convolution networks for biomedical image segmentation. arXiv preprint arXiv:2105.10559 .
- Mantovani, R.G., Rossi, A.L., Vanschoren, J., Bischl, B., Carvalho, A.C., 2015. To tune or not to tune: recommending when to adjust svm hyper-parameters via meta-learning, in: 2015 International Joint Conference on Neural Networks (IJCNN), Ieee. pp. 1–8.
- Mehralivand, S., Yang, D., Harmon, S.A., Xu, D., Xu, Z., Roth, H., Masoudi, S., Sanford, T.H., Kesani, D., Lay, N.S., et al., 2022. A cascaded deep learning–based artificial intelligence algorithm for automated lesion detection and classification on biparametric prostate magnetic resonance imaging. *Academic Radiology* 29, 1159–1168.
- Mehta, P., Antonelli, M., Ahmed, H.U., Emberton, M., Punwani, S., Ourselin, S., 2021. Computer-aided diagnosis of prostate cancer using multiparametric mri and clinical features: A patient-level classification framework. *Medical image analysis* 73, 102153.
- Molnar, C., 2020. Interpretable machine learning. Lulu. com.
- Nguyen, T.M., Wu, Q.J., 2012. Fast and robust spatially constrained gaussian mixture model for image segmentation. *IEEE transactions on circuits and systems for video technology* 23, 621–635.
- Orczyk, C., Barratt, D., Brew-Graves, C., Peng Hu, Y., Freeman, A., McCartan, N., Potyka, I., Ramachandran, N., Rodell, R., Williams, N.R., et al., 2021. Prostate radiofrequency focal ablation (proraf) trial: A prospective development study evaluating a bipolar radiofrequency device to treat prostate cancer. *The Journal of Urology* 205, 1090–1099.
- Padilla, R., Passos, W.L., Dias, T.L.B., Netto, S.L., da Silva, E.A.B., 2021. A comparative analysis of object detection metrics with a companion open-source

- toolkit. *Electronics* 10. URL: <https://www.mdpi.com/2079-9292/10/3/279>, doi:10.3390/electronics10030279.
- Qian, Y., Zhang, Z., Wang, B., 2021. Procdet: A new method for prostate cancer detection based on mr images. *IEEE Access* 9, 143495–143505.
- Ronneberger, O., Fischer, P., Brox, T., 2015. U-net: Convolutional networks for biomedical image segmentation, in: *International Conference on Medical image computing and computer-assisted intervention*, Springer. pp. 234–241.
- Rosenkrantz, A.B., Kim, S., Lim, R.P., Hindman, N., Deng, F.M., Babb, J.S., Taneja, S.S., 2013. Prostate cancer localization using multiparametric mr imaging: comparison of prostate imaging reporting and data system (pi-rads) and likert scales. *Radiology* 269, 482–492.
- Saeed, S.U., Yan, W., Fu, Y., Giganti, F., Yang, Q., Baum, Z., Rusu, M., Fan, R.E., Sonn, G.A., Emberton, M., et al., 2022. Image quality assessment by overlapping task-specific and task-agnostic measures: application to prostate multiparametric mr images for cancer segmentation. *arXiv preprint arXiv:2202.09798* .
- Saha, A., Hosseinzadeh, M., Huisman, H., 2021. End-to-end prostate cancer detection in bpmri via 3d cnns: Effects of attention mechanisms, clinical priori and decoupled false positive reduction. *Medical image analysis* 73, 102155.
- Sanford, T., Harmon, S.A., Turkbey, E.B., Kesani, D., Tuncer, S., Madariaga, M., Yang, C., Sackett, J., Mehralivand, S., Yan, P., et al., 2020. Deep-learning-based artificial intelligence for pi-rads classification to assist multiparametric prostate mri interpretation: A development study. *Journal of Magnetic Resonance Imaging* 52, 1499–1507.
- Schelb, P., Kohl, S., Radtke, J.P., Wiesenfarth, M., Kickingereeder, P., Bickelhaupt, S., Kuder, T.A., Stenzinger, A., Hohenfellner, M., Schlemmer, H.P., et al., 2019. Classification of cancer at prostate mri: deep learning versus clinical pi-rads assessment. *Radiology* 293, 607–617.

- Simmons, L.A., Kanthabalan, A., Arya, M., Briggs, T., Barratt, D., Charman, S.C., Freeman, A., Hawkes, D., Hu, Y., Jameson, C., et al., 2018. Accuracy of transperineal targeted prostate biopsies, visual estimation and image fusion in men needing repeat biopsy in the picture trial. *The Journal of urology* 200, 1227–1234.
- Snoek, C.G., Worring, M., Smeulders, A.W., 2005. Early versus late fusion in semantic video analysis, in: *Proceedings of the 13th annual ACM international conference on Multimedia*, pp. 399–402.
- Taspinar, Y.S., Cinar, I., Koklu, M., 2021. Classification by a stacking model using cnn features for covid-19 infection diagnosis. *Journal of X-ray science and technology*, 1–16.
- Trong, V.H., Gwang-hyun, Y., Vu, D.T., Jin-young, K., 2020. Late fusion of multimodal deep neural networks for weeds classification. *Computers and Electronics in Agriculture* 175, 105506.
- Turkbey, B., Mani, H., Shah, V., Rastinehad, A.R., Bernardo, M., Pohida, T., Pang, Y., Daar, D., Benjamin, C., McKinney, Y.L., et al., 2011. Multiparametric 3t prostate magnetic resonance imaging to detect cancer: histopathological correlation using prostatectomy specimens processed in customized magnetic resonance imaging based molds. *The Journal of urology* 186, 1818–1824.
- Van Sloun, R.J., Wildeboer, R.R., Mannaerts, C.K., Postema, A.W., Gayet, M., Beerlage, H.P., Salomon, G., Wijkstra, H., Mischi, M., 2021. Deep learning for real-time, automatic, and scanner-adapted prostate (zone) segmentation of transrectal ultrasound, for example, magnetic resonance imaging–transrectal ultrasound fusion prostate biopsy. *European urology focus* 7, 78–85.
- Vargas, H., Hötter, A., Goldman, D., Moskowitz, C., Gondo, T., Matsumoto, K., Ehdai, B., Woo, S., Fine, S., Reuter, V., et al., 2016. Updated prostate imaging reporting and data system (pirads v2) recommendations for the detection of clinically significant prostate cancer using multiparametric mri: critical evaluation using whole-mount pathology as standard of reference. *European radiology* 26, 1606–1612.

- Villers, A., Puech, P., Mouton, D., Leroy, X., Ballereau, C., Lemaitre, L., 2006. Dynamic contrast enhanced, pelvic phased array magnetic resonance imaging of localized prostate cancer for predicting tumor volume: correlation with radical prostatectomy findings. *The Journal of urology* 176, 2432–2437.
- Wang, A.Q., Dalca, A.V., Sabuncu, M.R., 2021a. Regularization-agnostic compressed sensing mri reconstruction with hypernetworks. *arXiv preprint arXiv:2101.02194* .
- Wang, H., Subramanian, V., Syeda-Mahmood, T., 2021b. Modeling uncertainty in multi-modal fusion for lung cancer survival analysis, in: *2021 IEEE 18th International Symposium on Biomedical Imaging (ISBI)*, IEEE. pp. 1169–1172.
- Wang, J., Wu, C.J., Bao, M.L., Zhang, J., Wang, X.N., Zhang, Y.D., 2017. Machine learning-based analysis of mr radiomics can help to improve the diagnostic performance of pi-rads v2 in clinically relevant prostate cancer. *European radiology* 27, 4082–4090.
- Wang, Y., Wang, D., Geng, N., Wang, Y., Yin, Y., Jin, Y., 2019. Stacking-based ensemble learning of decision trees for interpretable prostate cancer detection. *Applied Soft Computing* 77, 188–204.
- Weinreb, J.C., Barentsz, J.O., Choyke, P.L., Cornud, F., Haider, M.A., Macura, K.J., Margolis, D., Schnall, M.D., Shtern, F., Tempany, C.M., et al., 2016. Pi-rads prostate imaging–reporting and data system: 2015, version 2. *European urology* 69, 16–40.
- Wolpert, D.H., 1992. Stacked generalization. *Neural networks* 5, 241–259.
- Woźnicki, P., Westhoff, N., Huber, T., Riffel, P., Froelich, M.F., Gresser, E., von Hardenberg, J., Mühlberg, A., Michel, M.S., Schoenberg, S.O., et al., 2020. Multiparametric mri for prostate cancer characterization: Combined use of radiomics model with pi-rads and clinical parameters. *Cancers* 12, 1767.
- Yan, W., Yang, Q., Syer, T., Min, Z., Punwani, S., Emberton, M., Barratt, D., Chiu, B., Hu, Y., 2022. The impact of using voxel-level segmentation metrics on evaluating multifocal prostate cancer localisation, in: *Applications of Medical Artificial*

Intelligence: First International Workshop, AMAI 2022, Held in Conjunction with MICCAI 2022, Singapore, September 18, 2022, Proceedings, Springer. pp. 128–138.

Youn, S.Y., Choi, M.H., Kim, D.H., Lee, Y.J., Huisman, H., Johnson, E., Penzkofer, T., Shabunin, I., Winkel, D.J., Xing, P., et al., 2021. Detection and pi-rads classification of focal lesions in prostate mri: Performance comparison between a deep learning-based algorithm (dla) and radiologists with various levels of experience. *European Journal of Radiology* 142, 109894.

Zhou, W., Chen, Y., Liu, C., Yu, L., 2020. Gfnet: Gate fusion network with res2net for detecting salient objects in rgb-d images. *IEEE Signal Processing Letters* 27, 800–804.

## Supplementary Material

### *A.1 Derivation of decision rules based on PI-RADS*

PI-RADS is a guideline designed for standardising radiologist report of detecting and grading clinically significant prostate cancer on mpMR images. It aims to streamline the use of three MR modalities of T2W, DWI and DCE, with which DWI may be examined with one or more image modalities such as  $DWI_{hb}$  and ADC maps. DCE is considered if other clear practical benefits do not overweight its diagnostic value. A key feature of PI-RADS is that it has constantly been updated in response to emerging evidence. While it is out of the scope to discuss the practical use of the current version of PI-RADS, a binary classification version is derived from it for the purpose of demonstrating the proposed machine learning methodology.

To summarise, the current version of PI-RADS first defines dominant modality, T2W and DWI, for lesions found in TZ and PZ, respectively, before modifying the final grading, on a scale of 1-5, based on other image modalities. This is illustrated in the left diagram in Fig. 1 (left). As an example, considering a positive lesion with a score greater than or equal to 3 - negative otherwise - the binary classification used in this study is illustrated in the right diagram in Fig. 1 (right). It is noteworthy that, PI-RADS does not explicitly distinguish  $DWI_{hb}$  and ADC, since these are both diffusion-based modalities. Therefore, there has not been wide agreement when the presentation of disease differs between the two image modalities. For the purpose of quantifying between these two images types, this study considers either  $DWI_{hb}$  or ADC being greater than or equal to 3 is equivalent to DWI being greater than or equal to 3, while, for transition zone lesions, it needs both  $DWI_{hb}$  and ADC being greater than or equal to 3 in order to upgrade a negative lesion to a positive one. Table 7 summarize the condition and decision of lesion in peripheral zone.

$$\mathbf{R} = \begin{bmatrix} 0 & 0 & 0 & 0 & 1 & 1 & 1 & 1 \\ 0 & 0 & 1 & 1 & 0 & 0 & 1 & 1 \\ 0 & 1 & 0 & 1 & 0 & 1 & 0 & 1 \end{bmatrix}, \mathbf{d} = \begin{bmatrix} 0 \\ 1 \\ 1 \\ 1 \\ 0 \\ 1 \\ 1 \\ 1 \end{bmatrix} \quad (21)$$

where  $\mathbf{R} = [\mathbf{r}_1, \dots, \mathbf{r}_K]$  and  $\mathbf{d} = [d_1, \dots, d_K]^\top$ .

Given the constant condition vectors  $\mathbf{R}$  (Eq. 12), the resulted decisions  $\mathbf{d}^{(TZ)}$ ,  $\mathbf{d}^{(PZ)}$  and  $\mathbf{d}^{(WG)}$ , are summarised in Table 2, for TZ, PZ and WG lesions, respectively. The fitted hyperparameters,  $\hat{\alpha}$  and  $\hat{\beta}$ , can also be found in Table 2, for a linear stacking model and a nonlinear stacking model, respectively, using methods described in Sec.3.4.1.

#### A.2 Hyperparameters acceptance-rejection algorithm for non-linear stacking model

Since unnecessarily extreme values of the defined hyperparameters can lead to diverged optimisation during training, we determine the range of hyperparameters *upbeta* by solving the Eq. (15) in a least-square sense with sampled all possible conditions and decisions. An acceptance-rejection algorithm was followed to indirectly sample hyperparameter values for the nonlinear stacking models, as outlined in Algorithm 1. In this application, these sampled values were used as hyperparameters  $\beta$  for the training of HyperCombiner networks with the nonlinear stacking model. A set of  $N$  samples

$C$	$p(C   \tau = 1)$	$p(C   \tau = 2)$	$p(C   \tau = 3)$	$p(C)$
PZ	negative	negative	negative	NEGATIVE
PZ	negative	negative	positive	POSITIVE
PZ	negative	positive	negative	POSITIVE
PZ	negative	positive	positive	POSITIVE
PZ	positive	negative	negative	NEGATIVE
PZ	positive	negative	positive	POSITIVE
PZ	positive	positive	negative	POSITIVE
PZ	positive	positive	positive	POSITIVE

Table 7: Example condition vectors and decisions for peripheral zone (PZ) lesions,  $\tau=1,2$  and 3 represent T2W,  $DWI_{hb}$  and ADC, respectively.

were pre-computed for being randomly sampled in each training iteration. During inference, the grid search was conducted among all these hyperparameter values for rule discovery.

---

**Algorithm 1:** Rejection sampling for nonlinear stacking model

---

**Data:** Required sample size  $N = 2^8$   
**Result:** Sampled hyperparameter set  $\{\beta_1, \dots, \beta_N\}$

- 1 Initialise counter  $n = 1$ , a constant condition vector set  $\mathbf{R}$
- 2 **while**  $n \leq N$  **do**
- 3     **STEP1:** Convert  $n$  to an 8-bit binary number as  $\mathbf{d}_n$
- 4     **STEP2:** Compute for  $\beta_n$
- 5     **for**  $i=0, i++, i \leq 10^4$  **do**
- 6          $\hat{\mathbf{d}}_n = \sigma([\mathbf{R}^\top, \mathbf{1}] \cdot \beta_n)$
- 7          $loss = -\sum p(d_{k,n}) \cdot \log p(\hat{d}_{k,n})$
- 8          $\beta_n \leftarrow \beta_n + \nabla l(\beta_n)$
- 9     **end**
- 10    **STEP3:**
- 11    **if**  $\|\mathbf{d}_n - \hat{\mathbf{d}}_n\|_2^2 \leq \frac{\eta^2}{8}$  **then**
- 12         $n++$
- 13    **end**
- 14 **end**

---

<sup>5</sup> $\eta$  is a small number that makes sure the l2 difference between  $\mathbf{d}$  and  $\hat{\mathbf{d}}$  is same, here,  $\eta = 0.5$ .